

Wettability and sp^2/sp^3 ratio effects on supercapacitor performance of N-doped hydrogenated amorphous Carbon Nanofoam

Subrata Ghosh^{1,2*}, Giacomo Pagani¹, Andrea Macrelli¹, Alberto Calloni³, Gianlorenzo Bussetti³, Andrea Lucotti⁴, Matteo Tommasini⁴, Raffaella Suriano⁵, Valeria Russo¹, Agnieszka M. Jastrzębska², Cinzia Casiraghi⁶, Andrea Li Bassi¹, Carlo S. Casari^{1*}

¹Micro and Nanostructured Materials Laboratory – NanoLab, Department of Energy, Politecnico di Milano, via Ponzio 34/3, Milano, 20133, Italy

²Faculty of Mechatronics, Warsaw University of Technology, sw. Andrzeja Boboli 8, 02-525 Warsaw, Poland

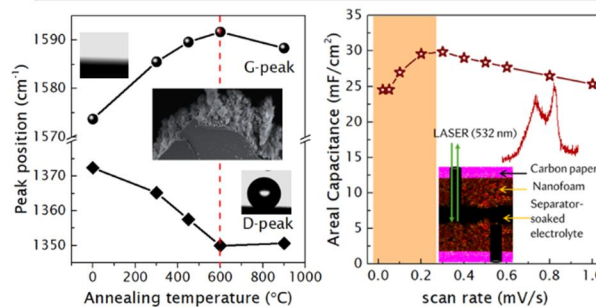
³Solid Liquid Interface Nano-Microscopy and Spectroscopy (SoLINano-Σ) lab, Department of Physics, Politecnico di Milano, Piazza Leonardo da Vinci 32, 20133 Milano, Italy

⁴Department of Chemistry, Materials and Chemical Engineering, “Giulio Natta” Politecnico di Milano, Milano, 20133, Italy

⁵Laboratory of Chemistry and Characterization of Innovative Polymers (ChIPLab), Department of Chemistry, Materials and Chemical Engineering “Giulio Natta”, Politecnico di Milano, Piazza Leonardo da Vinci 32, 20133 Milano, Italy

⁶Department of Chemistry, University of Manchester, Manchester, M13 9PL, UK

Abstract: Pulsed laser-deposited amorphous carbon nanofoams could be a potential candidate for electrochemical energy storage applications due to their properties such as ultralightweight, huge volumetric void fractions, and co-existence of sp , sp^2 and sp^3 carbon hybridization. It is known that the charge-storage of carbon nanostructures containing disordered sp^2 -domains is determined by the wettability, surface area, and porosity of carbon nanostructures. However, their charge-storage performance is limited to the areal capacitance of the order of a few mF/cm^2 . We enhanced the supercapacitor performance of nitrogen-doped amorphous carbon nanofoam by engineering its wettability and sp^2 -C/ sp^3 -C ratio by vacuum annealing. The specific capacitance was enhanced around fifty times and the widened voltage of the device increased from 0.8 to 1.1 V compared to as-grown nanofoam. In addition, we examined for the first time the initial increase in specific capacitance of the aqueous symmetric supercapacitor with respect to the scan rate, employing *in-situ* measurements coupling Raman spectroscopy and electrochemistry. We attribute this effect, although observed in previous literatures but unexplained, to the electrochemical activation induced by structural changes during the charge storage performance. This optimization of pulsed laser-deposited carbon nanofoam may open an avenue for fabricating lightweight and porous nanostructures for advanced macro-to-micro-supercapacitor devices.



Keywords: Nanocarbons; wettability; graphitic quality; *in-situ* spectro-electrochemistry; supercapacitor

Corresponding author email: subrata.ghosh@pw.edu.pl (S.G.) and carlo.casari@polimi.it (C.S.C.)

ORCID ID: [0000-0002-5189-7853](https://orcid.org/0000-0002-5189-7853) (S. G.); [0009-0001-7437-545X](https://orcid.org/0009-0001-7437-545X) (G.P.); [0000-0002-5307-5124](https://orcid.org/0000-0002-5307-5124) (A. M.); [0000-0002-7389-2703](https://orcid.org/0000-0002-7389-2703) (A.C.); [0000-0001-8556-8014](https://orcid.org/0000-0001-8556-8014) (G.B.); [0000-0003-2148-1408](https://orcid.org/0000-0003-2148-1408) (A.L.); [0000-0002-7917-426X](https://orcid.org/0000-0002-7917-426X) (M.T.); [0000-0002-7448-359X](https://orcid.org/0000-0002-7448-359X) (R.S.); [0000-0001-9543-0422](https://orcid.org/0000-0001-9543-0422) (V.R.); [0000-0001-7185-0377](https://orcid.org/0000-0001-7185-0377) (C. C.); [0000-0001-8900-1859](https://orcid.org/0000-0001-8900-1859) (A.M.J.); [0000-0002-1265-4971](https://orcid.org/0000-0002-1265-4971) (A. L. B.); [0000-0001-9144-6822](https://orcid.org/0000-0001-9144-6822) (C.S.C.)

1. Introduction

Supercapacitors have established their own ground and are anticipated as one of the promising electrochemical energy storage devices for the clean energy technological solution owing to their excellent power density and cycle life. [1][2] One of the biggest challenges in the development of this technology for both the academic and industrial communities is to enhance the energy density to be able to compete with batteries. The streamlined research focuses are the development of advanced electrode materials design, the investigation of the best electrolytes, as well as the study of the best combination of them.[3][4][5][6] Among the electrode materials, carbon-based nanostructures are promising as they offer excellent structural quality, tuneable porosity, and the possibility to be doped or decorated with other systems to form nanostructures.

It is well known that carbon nanostructures exist in the form of fully sp^2 -bonded, fully sp^3 -bonded, and their mixtures. The pure sp^2 -bonded carbon, graphene, unfortunately failed to reach its theoretical capacitance (550 F/g) despite high surface area of 2630 g/cm² and excellent structural quality.[7] On the other hand, the sp^3 -bonded carbon allotrope, diamond, is well-known to provide an excellent electrochemical stability over the widened potential window. However, it also shows poor charge-storage capacity as the main drawback for use in supercapacitors.[8][9] Thus, there is an increasing trend to prepare sp^2 - sp^3 carbon nanostructures for enhanced storage performance.[10] Recent studies claim nanoporous carbons containing small graphene (sp^2 -hybridized) flakes with high structural disorder,[11] and less than one nanometer-sized pores[12] are promising as high-performance supercapacitor electrodes. Factors influencing the performance of carbon-based supercapacitors or electric double-layer capacitors are wettability, structural quality, porosity, surface area, type of hybridization (sp , sp^2 and sp^3), and heteroatom doping.[1][2][13][14][4][15] It should be noted that tuning one factor independently while keeping constant the others is experimentally challenging. For example, while graphene oxide is annealed, not only the porosity and the electrical conductivity change but also the sp^2 -C-to- sp^3 -C ratio, associated to the amount of oxygen functional groups, and hence the structure is also changing.[16] Regarding the carbon nanostructures such as carbon nanotubes, vertical graphenes etc, its hydrophobic nature resists the electrode/electrolyte interaction. Hence, tuning the wettability by heteroatom doping or oxygen functionalization can make it hydrophilic and is one of the adoptable strategies to improve the charge-storage performance.[14][4][6] Heteroatom doping is also influential to improve the charge-storage/transfer kinetics, to contributes pseudocapacitance, and to increase the double-layer capacitance.[4] Machine learning-assisted design of porous carbon nanostructures containing nitrogen and oxygen functional groups has been anticipated as promising to design optimized supercapacitor electrode.[13] However, it has been reported that reduced graphene oxide annealed at 200 °C with specific structure in terms of carbon/oxygen ratio, and electrical conductivity exhibits higher specific capacitance than the pristine one and reduced graphene oxide annealed at more than 200 °C.[16] This result suggests that the carbon nanostructures with optimized properties is crucial to obtain the high charge-storage performance while used as supercapacitor electrode.

Amorphous carbons with plenty of electrochemical active sites and local structural disorder can be utilized as an energy storage electrode. However, poor electrical conductivity limit its use as electrode.[17] Thus, one needs to tailor the structure for better charge transport and electrochemical stability in parallel to the enhancement in charge storage capacity. A free-standing amorphous carbon film was also prepared by chemical vapor deposition, which was transferred from the Ni substrate to the desired one to fabricate a supercapacitor device, but the areal capacitance was limited within 0.28 mF/cm² at 50 mV/s.[17] In this context, pulsed laser-deposited amorphous carbon nanofoam could be a potential electrode material as it consists of sp , sp^2 and sp^3 hybridizations. It is also lightweight, with less-ordered structure, more than 90% porosity, and superhydrophilicity.[18][19] However, our previous investigations show that an aqueous supercapacitor composed of amorphous carbon foam, which was grown directly on a current collector by pulsed laser deposition at room temperature, delivers the areal capacitance of around 1 mF/cm² at 0.1 V/s, in spite of being hydrophilic and highly disordered.[19] We also highlight that one can find significant reports on carbon nanostructures or other nanostructures, where the material with lower thickness or low mass loading delivered

higher specific capacitance.[20][21] However, ultrathick materials with high charge-storage performances are much appreciated to be used for real applications.

Thus, there is a room to improve the charge-storage performance of ultrathick carbon nanofoam further, which is the focus of the current research. In the present work, hydrogenated amorphous carbon nanofoam containing nitrogen was synthesized directly on the current collector by pulsed laser deposition at room temperature, to avoid any use of binders and conductive agents. The wettability and sp^2 -C/ sp^3 -C ratio of the nanofoams were tuned by vacuum annealing at different temperatures. The changes in wettability, sp^2 -C/ sp^3 -C ratio, and functionalities were monitored by water contact angle measurement, Raman and Fourier-transform infrared (FTIR) spectroscopy, and X-ray photoemission spectroscopy (XPS). Finally, an aqueous symmetric supercapacitor device was assembled to investigate the charge storage performance of those nanofoams and correlate them with their physico-chemical characteristics. While investigating the charge-storage performance, we observed an initial increase of capacitance with respect to the scan rate, which is rare but observed in previous reports on nanoporous gold/MnO₂ hybrid electrode[22], MnO₂ nanorods on carbon nanotubes,[23] and metal-free MXene[24]. Therefore, *in-situ* Raman spectro-electrochemistry of the prototype aqueous symmetric supercapacitor was performed and the changes in graphitic quality due to the electrochemical activation is attributed for the initial increase in specific capacitance with respect to the scan rate. This result shows that nanofoam with optimized properties can be a potential electrode for binder-free thin-film supercapacitor applications.

2. Experimental methods

2.1. Synthesis of carbon nanofoam

Binder-free carbon nanofoams were directly grown on the carbon paper and Si substrate using the pulsed laser deposition at room temperature. The target used was 1-inch graphite and the ablation was carried out using a Nd:YAG pulsed nanosecond-laser (2nd harmonic at 532 nm, pulse duration 5-7ns, repetition rate 10 Hz). Two-step deposition was carried out: a buffer layer was formed at the deposition pressure of 5 Pa for 2 min, followed by the deposition of a porous structure for 30 min at 300 Pa under the mixture of 95% nitrogen and 5% hydrogen background gas and the laser pulse energy of about 416 mJ with a fluence of 6.5 J/cm². Prior to the deposition, the chamber was evacuated down to 10⁻³ Pa using a rotary pump connected in series with a turbomolecular pump. The distance between the substrate and the bottom target was 40 mm.

As deposited nanofoams were treated at various temperatures of 300, 450, 600 and 900 °C in a tube furnace for 1 hour under vacuum to modify the sp^2 -C/ sp^3 -C ratio and functionalities. Ramping rate to reach the desired temperature was 4 °C/min and the pressure during the annealing was maintained at 5×10⁻³ Pa by rotary and turbomolecular pump. For the functionalization, the optimized carbon nanofoam was dipped into 8M HNO₃ solution for 7.30 hours at the temperature of 120 °C, then it was washed several times with deionized water until the pH of the solution reached 6, and finally it was dried in an oven at around 90 °C.[25]

2.2. Morphological and structural characterization.

A field-emission scanning electron microscope (FE-SEM, ZEISS SUPRA 40, Jena, Germany) was employed to investigate the morphology of the composite, where an *in-lens* detector operates in a high vacuum. Energy dispersive X-ray spectra (EDXS) were recorded at the acceleration voltage of 20 kV, using AZtec software for elemental analysis, volumetric void fraction estimation, and mass density. The instrument was equipped with a Peltier-cooled silicon drift detector (Oxford Instruments).

X-ray photoelectron spectroscopy (XPS) was utilized to investigate the elemental analysis and bonding environment of the pristine and annealed carbon nanofoams. XPS data were collected using a non-monochromated X-ray source using a Mg anode (photon energy 1253.6 eV), maintained at a power of 200 W, and pressure of around 1×10⁻¹⁰ Torr. The kinetic energy of the photoemitted electrons was recorded using a hemispherical analyser with a 150 mm mean radius, PHOIBOS150 from SPECS GmbH. The spectra were

acquired with a pass energy of 20 eV, with an energy resolution of 0.9 eV (full width half maximum, FWHM). Peaks were fitted after Shirley background subtraction using CasaXPS software, and at.% of elemental compositions were extracted from peak area ratios after correction by Scofield relative sensitivity factors (C=1.0, N=1.77, O=2.85).[26] For C1s, the asymmetric sp^2 -C peak (calibrated at 284.8 eV) was fitted with Gaussian-Lorentzian lineshape (GL(30)) with asymmetric factor (T200) and other symmetric carbon peaks with GL(30) by setting the range of FWHM to 1.2–2 eV. The FWHM of oxygenated carbon peaks, deconvoluted O1s peaks, and deconvoluted N1s peaks were set to 1.8–2.2 eV. The sp^3 -C peak was generally shifted by 0.7–1 eV from sp^2 -C and hydroxyl/ether, carbonyl, and carboxylic groups were shifted approximately 1.5, 3, and 4.5 eV higher, respectively.

Micro-Fourier Transform Infrared (FT-IR) measurements on the carbon foam deposited on silicon were performed using the Nicolet Nexus interferometer coupled with a Thermo-Nicolet Continuum infrared microscope and a cooled MCT detector (77 K). The films deposited on silicon were measured in transmission through two co-axial Cassegrain 15× infrared objectives (one for focalizing the IR beam, the other for the collection of the transmitted light). The analyzed area was approximately 200 μm x 200 μm.

The Raman spectra of all samples were recorded by Renishaw *In via* Raman spectrometer, UK. The spectra were acquired using a 514.5 nm laser with a power of 0.4 mW on the sample, a 1800 line/mm grating spectrometer, a 50× objective lens, and 20 accumulation (10 s each).

2.3. Wettability measurement

Wettability measurements were performed using an OCA 15plus instrument (Dataphysics Co., Filderstadt, Germany), equipped with a CCD camera to capture side views of drop images, and a 500 μL Hamilton syringe to dispense water droplets. Water for chromatography (LC-MS Grade, LiChrosolv®) supplied by Merck (KGaA, Darmstadt, Germany) was used as a probe liquid. Measurements were performed at room temperature, using the sessile drop method. For static measurements, the Young–Laplace equation was employed to determine the contact angles by interpolating the contour side droplet, using the OCA20 instrument software. The dispensed volume for static measurements was 2 μL. Regarding dynamic measurements, the tangent method at the left and right three-phase points of the side droplet image was employed to obtain the contact angle measurements over time and the dispensed volume was 1 μL.

2.5. Electrochemical measurements.

The electrochemical performances of the nanocomposites were investigated in a 2-electrode configuration using a Swagelok Cell (SKU: ANR-B01, Singapore) and 6M KOH as the electrolyte. The hydrophobic propylene microporous membrane (Celgard 2500) was modified by a two-step process: soaking with acetone at 20 °C for 5 min followed by dipping in aqueous 6M KOH solution at 20 C for 1 h.[27] The cell was assembled by sandwiching separator-soaked-electrolytes between the carbon nanofoam grown on carbon paper. Prior to the test, electrodes and a modified separator were dipped into the electrolyte solution for several hours. Cyclic voltammogram, charge-discharge tests, and electrochemical impedance spectra were recorded using a PALMSENS4 electrochemical workstation. Before recording the original data, the prototype cells were scanned at 100 mV/s scan rate for 1000 cycles. The cyclic voltammetry at different scan rates ranging from 0.02 to 1 V/s and charge-discharge at different current densities of 150 μA to 2 mA were carried out. The areal capacitance was calculated from a cyclic voltammogram using the equation: $C_{areal} = \int I dV / A \cdot \nu \cdot V$, where I is the current, ν is the scan rate, A is the geometric area of the electrode, and V is the voltage of the device. Energy density (E) and power density (P) of devices were estimated via the relations of $E = 0.5 C_{areal} V^2$ and $P = (E \cdot \nu) / V$, respectively. Single electrode capacitance = 4 × device capacitance. The volumetric capacitance of electrode materials was estimated by dividing the areal capacitance by the total height of two symmetric nanocomposite electrodes. The gravimetric capacitance of the device is equal to volumetric capacitance divided by estimated mass density. The areal capacitance of the device is also calculated from the charge-discharge profile using the

relation: $C_{areal} = \frac{I_d \cdot \int V(t) \cdot dt}{A \cdot \int v \cdot dV}$. The electrochemical impedance spectroscopy was conducted in the frequency range of 1 Hz to 0.1 MHz at open circuit potential with a 10 mV *a.c.* perturbation. The relaxation time constant (τ_0) was estimated from the corresponding frequency (f_0) at -45° phase angle using the equation of $f_0 = 1/\tau_0$.

For the *in-situ* Raman spectro-electrochemical measurements, two similar electrodes were separated by the electrolyte-soaked separator. A hole with diameter of 0.1 cm was made on the top electrodes and separator such that laser can reach the bottom electrode without any interaction with top electrode and separator. A similar size of hole was also created on the bottom electrode to maintain the same geometrical area of both electrodes. A thin glass slide was placed on the top electrode and the full device was sealed with Kapton tape. The electrical connections between the electrodes and the potentiostat were given by platinum wires since Cu wire was corroded by KOH electrolyte. For this study, a Renishaw *In-Via* micro-Raman spectrometer with a diode-pumped solid-state laser (wavelength of 532 nm) and an 1800 grooves/mm grating was used. The laser was focused on the sample using a 50× long working distance objective and the incident power on the sample was 1.75 mW to appraise the threshold for laser-induced degradation. Each spectrum was acquired using 5 accumulations, 10 s each.

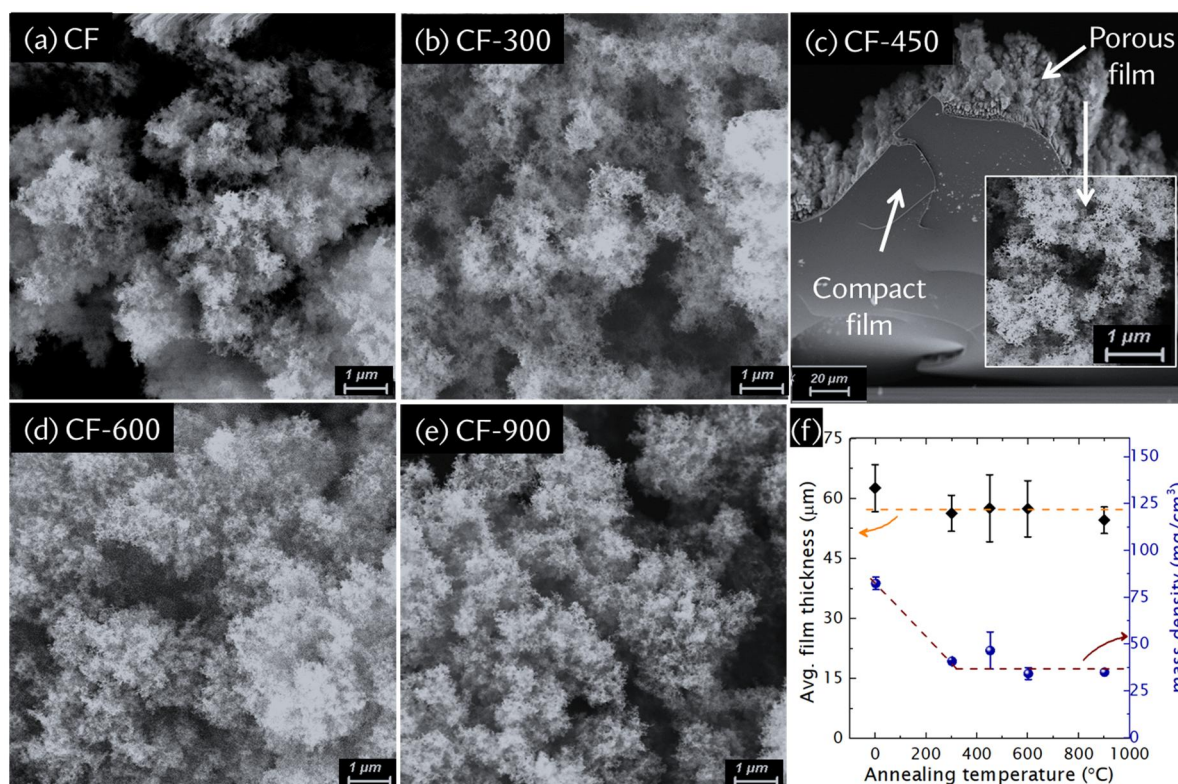


Figure 1: Scanning electron micrographs of (a) pristine nitrogenated amorphous carbon nanofoam (CF) and annealed nanofoams at (b) 300 °C, (c) 450 °C, (d) 600 °C, and (e) 900 °C. (f) Plot of average thickness and mass density of pristine and annealed nanofoams. Figure 1(c) is taken from the backside of nanofoam whereas inset represent the top-view as images for all nanofoams.

3. Results and Discussions

The morphology of as-grown and annealed (at increasing temperature) carbon nanofoam is shown in Figure 1(a-e). As it can be seen, the porous structure is clearly observed. No observable changes in the morphology of annealed carbon nanofoam is noticed, as compared to the pristine sample ensuring the morphological preservation under vacuum annealing even at high temperature of 900 °C. The nanofoam studied here is composed of a compact film and a porous film, as it can be seen from Figure 1c, where the backside view shows the porous nanofoam grown onto compact layer. The compact film provides better adhesion with the current collector (carbon paper in our case) and is efficient for the electron transportation, whereas the highly porous structure is responsible for the charge-storage at the interface of electrode/electrolyte via double layer formation. Total average thickness of all nanofoam is estimated to be around 57 μm (Figure 1f), which is much

higher than many electrode materials reported (below 10 μm or even in nanometer scale) for supercapacitor application.[20][21][28].

As it can be seen from the EDXS layered image (Figure 2a), oxygen and nitrogen are uniformly deposited on the carbon matrix. The quantitative information on the presence of carbon, oxygen, and nitrogen is estimated from EDXS and XPS measurements (Figure 2b-c). The discrepancy in the atomic concentration of elements obtained from the two techniques is due to their own limitations. EDX probes the volume of the film while XPS is more sensitive to the surface. In general, both techniques reveal the increase of the carbon content with annealing temperature whereas the content of functional groups (oxygen and nitrogen) decreases (Figure 2c). For CF-900, the nitrogen content is extremely low. It should be noted that the carbon nanofoams also contain hydrogen, as they were synthesized under $\text{N}_2\text{-H}_2$ environment (discussed later in the section of Raman spectroscopy and XPS) and also due to the unwanted moisture adsorption on the surface. Since porosity is one of the key factors for supercapacitor applications, the quantitative estimation of the porosity of our materials (volumetric void fraction, in our case), the elemental compositional ratio, and the mass density of as-grown nanofoams are evaluated by EDXS measurements coupled with the EDDIE software (the measurement details can be found in the Experimental section and in our previous report[19], and the fitted spectra using the EDDIE software are provided in Figure S1).[19] By providing the input of elemental composition details and Si substrate reference, the mass density of as-grown pristine nanofoam is estimated to be 77 mg/cm^3 . However, once annealed under vacuum, the estimated mass density drops to around 42 mg/cm^3 for all annealed carbon foams. The mass density of the nanofoam is in the range of ultralow density materials ($<300 \text{ mg/cm}^3$), and hence our material can be referred to as an ultralow dense carbon nanofoam. Using the mass density of nanofoams and comparing with that of graphite (2.2 g/cm^3 as a reference), the estimated volumetric void fraction of the nanofoam is in the range of 95-98%, confirming its highly porous structure.

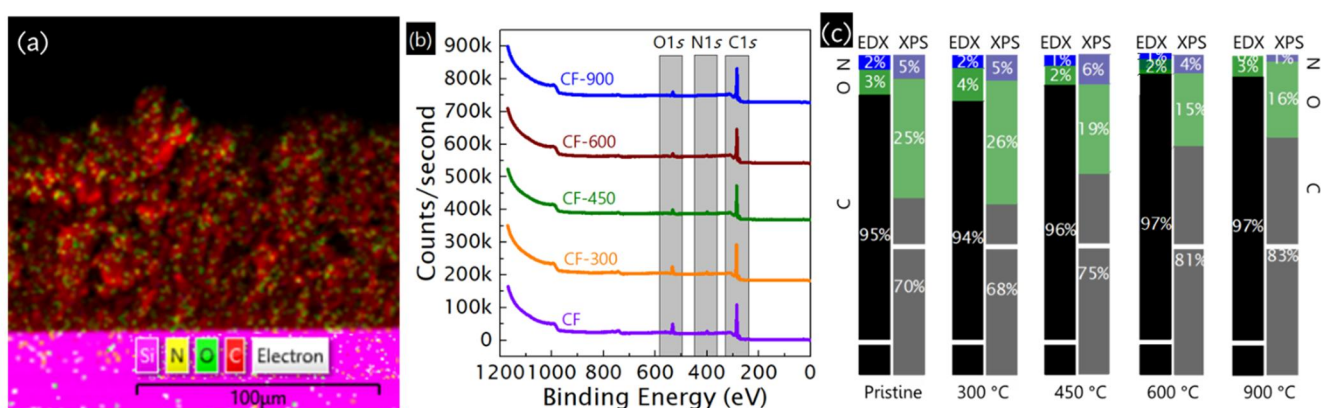


Figure 2: (a) Representative electron dispersive layered X-ray image of amorphous carbon nanofoam showing uniform distribution of nitrogen and oxygen over carbon surface. (b) XPS survey spectra of pristine and annealed carbon nanofoams. (c) Elemental compositional ratio of carbon, nitrogen, and oxygen of pristine and annealed nanofoams obtained from EDXS and XPS techniques.

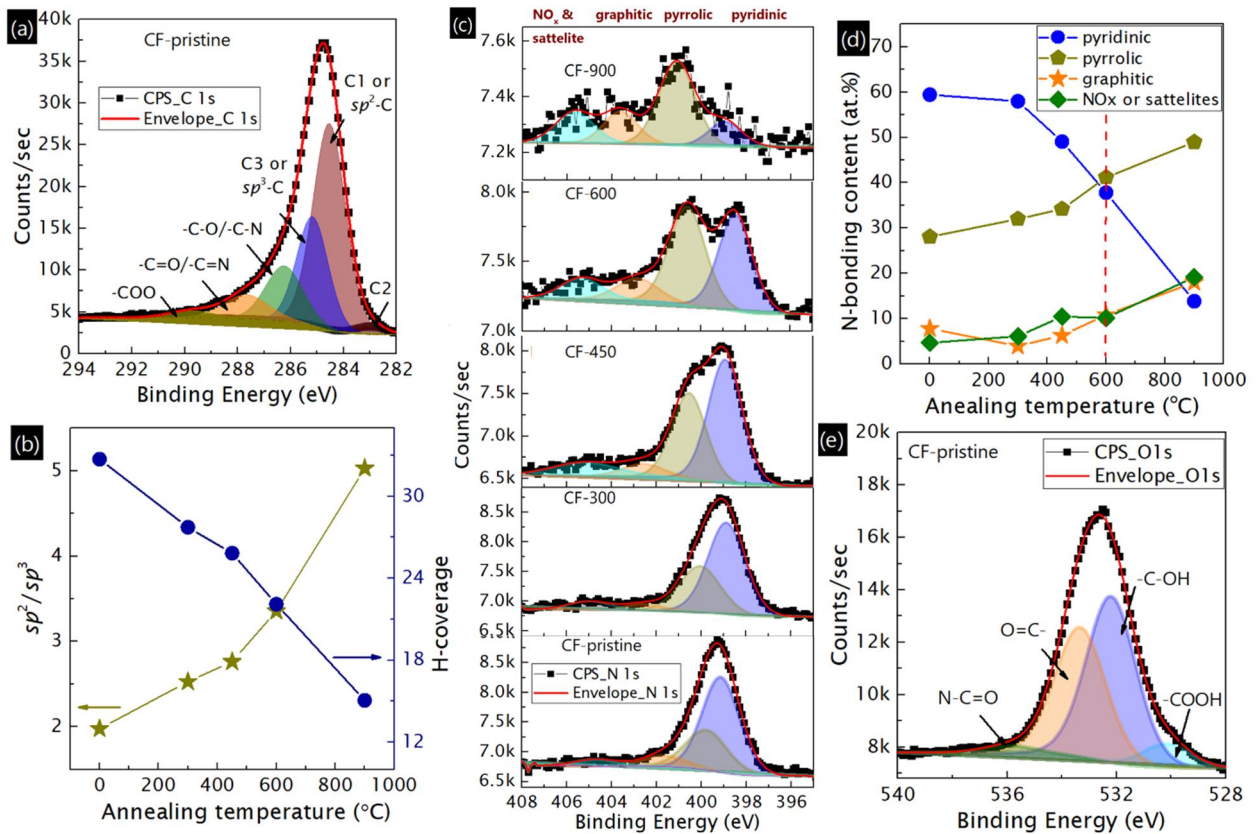


Figure 3: XPS results. (a) C1s spectrum of CF-pristine with deconvoluted peaks, (b) variation of sp^2/sp^3 content and H-coverage of CF with annealing temperature, (c) N1s spectrum with deconvoluted peaks, and (d) variation of N-bonding contents of pristine and annealed CFs. (e) O1s spectrum of CF-pristine with deconvoluted peaks.

For a better understanding of the structural improvement of the nanofoam upon annealing, the core-level C1s spectra of as-grown and annealed carbon nanofoams are further analysed and shown in Figure 3a and Figure S2a-d of supplementary material. The C1s spectra consist of sp^2 -C (at around 284.5 eV), sp^3 -C (at around 285.2 eV), the peak at around 283 eV (C2) associated with sp -C and vacancy defects, and the peaks associated with functional groups in the range of 286-290 eV (see Table S1 of supplementary material). The impact of annealing on the sp^2/sp^3 ratio is found to increase with respect to the annealing temperature (Figure 3b). In our case, the sp^3 -C for pristine sample consists of sp^3 C-C and sp^3 C-H, which is difficult to distinguish from XPS. We also estimated the H-content using the equation of $H - coverage(\%) = \frac{sp^3-C \times 100}{sp^2-C + C2 + sp^3-C}$. [29][30] and found that the H-content of nanofoam decreases as annealing temperature increase. Thus, the increase of sp^2/sp^3 ratio and reduction of H-content upon annealing (Figure 3b) is an indirect indication of structural improvement via transformation of sp^3 -C to sp^2 -C and sp^3 C-H to sp^3 C-C in the structure. Apart from C1s spectra evolution, we observe a distinct evolution of N-bonds from the N1s spectra upon annealing of pristine nanofoams (Figure 3c). Each N-bonding is extracted from the N1s spectrum by deconvoluting it into four configurations: pyridinic-N (at around 399 eV), pyrrolic-N (at around 400 eV), graphitic-N (at around 402 eV), and NO_x and satellite peaks (at around 405 eV) (Table S2 of supplementary material). Among the N-bonds, pyridine/pyrrole-N defects provide additional ion adsorption sites, improve the wettability, enhance the ion diffusion kinetics, and hence improve the overall charge-storage performance of the electrode material, whereas graphitic-N improves the electrochemical stability.[4] These N-bonds are well known to contribute pseudocapacitance, quantum capacitance, and increase the double-layer capacitance.[31] After extracting those N-bonding contributions, it has been seen that pyridinic-N content decreases and other N-bonds increase with the increasing annealing temperature (Figure 3d). From Figure 3c, it can also be seen that the pyrrolic-N and graphitic-N started to be more prominent from the CF annealed at or above 450°C. For CF-600°C, almost an equal amount of pyridinic-N and pyrrolic-N is observed (Figure 3d). The O1s spectrum of pristine carbon foam with deconvoluted peaks such as COOH-group, C-OH group, C=O group, and N-C=O group is shown in Figure 3e and Figure S2(e-h) in

the supplementary material (see also Table S3). Although a clear trend in each oxygen functional group content has not been seen, an evolution of -C=O group over C-OH group is noticed, and N-C=O content is found to be increased upon annealing.

Fourier Transform Infrared absorption spectroscopy is another analytical technique used to highlight the presence of functional groups within the carbon foam (Figure 4a). By analysing the FT-IR spectra collected in transmission on the carbon foam films deposited on silicon, we observe a weak band around 2150 cm^{-1} , which we assign to the stretching vibrations of C≡N or C≡C bonds. We also observe a significant increase of the background of the FT-IR spectra with the increasing annealing temperature. This is presumably related to scattering effects and/or increased light absorption due to the changing electronic properties of the annealed foams. Another important evidence comes from the C-H stretching region (just below 3000 cm^{-1}). The aliphatic C-H stretching bands (with sp^3 carbon) are quite intense in the pristine carbon nanofoam and in the sample annealed at 300 °C , but they tend to vanish for samples annealed at higher temperatures due to the loss of hydrogenated species, which is in a good agreement with XPS results. The FT-IR observations confirm the evidence collected using Raman spectroscopy regarding the restructuring of the carbon film with increasing annealing temperature, which implies the gradual increase of the sp^2 -content organized in honeycomb domains (as discussed below).

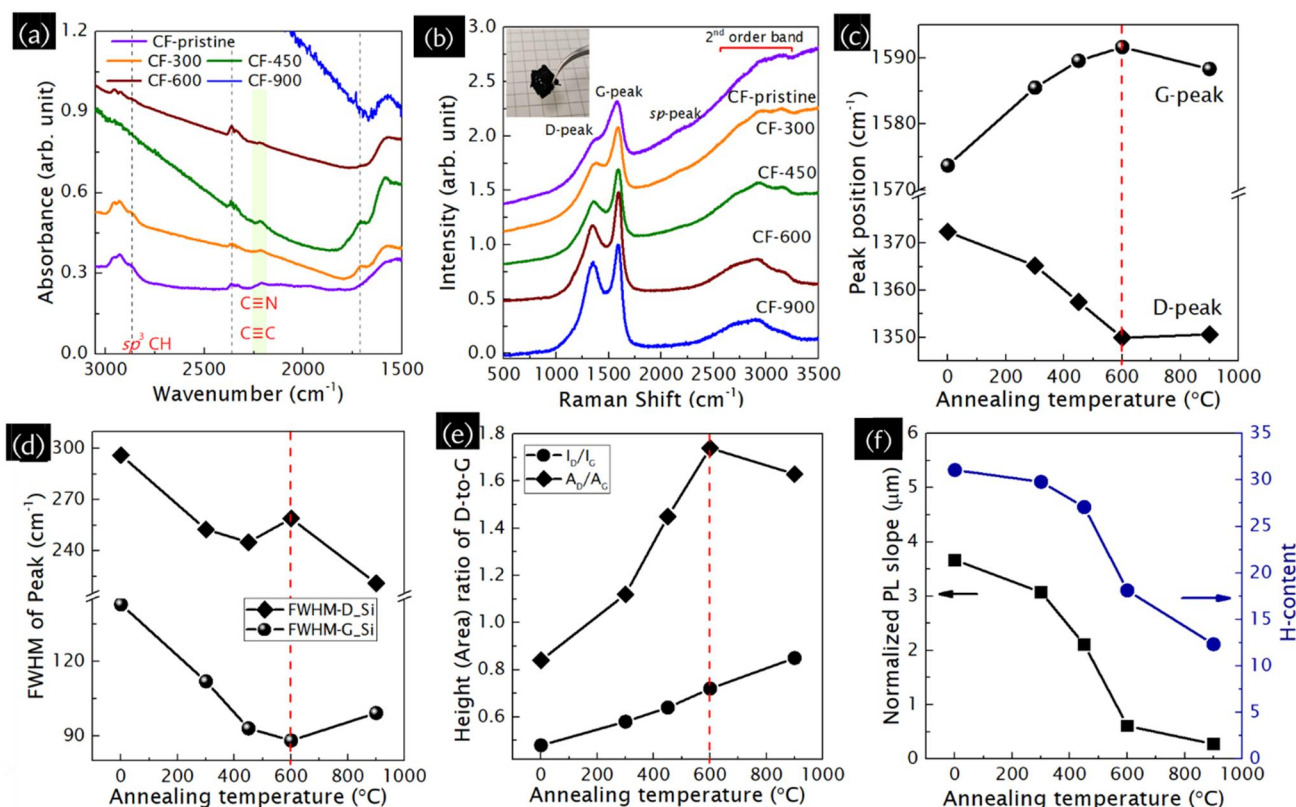


Figure 4: Evolution of (a) FT-IR spectra and (b) Raman spectra of frontside or porous-side of CF with annealing temperature. Plot of (c) position of D-peak and G-peak, (d) FWHM of D-peak and G-peak, (e) I_D/I_G and A_D/A_G , and (f) normalized photoluminescence or PL slope with respect to the annealing temperature. For the analysis of Raman spectra in (b-e), Raman spectra were recorded in three different positions and averaged out to extract the Raman parameters (laser wavelength is 514 nm).

In order to validate the structural improvement of nanofoams upon annealing, we investigated the Raman spectra from the porous side and also the compact side.[32][33][34] The carbon nanofoams are free-standing (see the inset of Figure 4b), and the annealed film can be easily detached from the silicon substrate due to the poor adhesion. Figure 4(b) shows the structural evolution of Raman spectra recorded from the porous side or top of the carbon foam. Typically, the Raman spectrum of carbon foam consists of D-peak and G-peak, with a very weak contribution of sp -peak and followed by a broad band in the high-frequency range, which is the typical spectrum of amorphous carbon.[35] To investigate the structural changes in nanofoam upon annealing, we fit

the D-peak with Lorentzian function and the asymmetric G-peak with Breit–Wigner–Fano function. In The clear observations on the annealing effect of carbon foams are the reduction in photoluminescence (PL) background, and changes in peak position, FWHM, and intensity or height (area) ratio of D-to-G peak (I_D/I_G and A_D/A_G) (Figure 4c-f). The peak position of D-peak, FWHM of D- and G-peak, and the normalized PL slope of carbon foams decrease, whereas the G-peak position, I_D/I_G and A_D/A_G are found to increase upon annealing until the sample CF-600 ensures the structural ordering of nanofoam. For CF-900, the increasing or decreasing trend of above parameters was flipped. A closer inspection of the spectra shows a weak hump at around 1150 cm^{-1} in CF-600 (an enlarged and clearer version can be seen from Figure S3a of supplementary material), which could be an indication of pentagon-heptagon structures[36] in the carbon foam. Since the D-peak is quite broad for all samples, the peak at 1150 cm^{-1} became very weak or shadowed under the D-peak. We have also estimated the H-content from normalized PL slope employing the similar empirical formula used for hydrogenated α -C. [33]. We found a good agreement of H-content estimation from Raman spectra with the H-coverage estimation from XPS (Figure 3b). These changes in Raman spectra can be attributed to the sp^3 -C to sp^2 -C transformation, sp^3 C-H to sp^3 C-C transformation, reduction of N-content, and change in N-bonding as it is observed from XPS results.

Moreover, we found an interesting result on the Raman spectra recorded from the backside of the free-standing film, which is basically the compact film as indicated in Figure S3b of supplementary material. The backside Raman spectra are quite different from the Raman spectra acquired on the porous side. For instance, the deconvolution of first-order Raman spectra of CF-600 from compact-side resulted in D-peak at around 1362 cm^{-1} with FWHM of 325 cm^{-1} and G-peak at around 1570 cm^{-1} with FWHM of 152 cm^{-1} in contrast to those from porous-side (D-peak at around 1350 cm^{-1} with FWHM of 259 cm^{-1} and G-peak at around 1591 cm^{-1} with FWHM of 88 cm^{-1}). The difference in the Raman spectra of carbon foams between compact side and porous side is obvious due to the different morphology and different localized heating gradient during annealing as the compact side is supported by the substrate. Moreover, we also noticed the presence of curvature peaks[37] at around 400 and 700 cm^{-1} , and sp C \equiv N peak at around 2210 cm^{-1} is clearly observed in both CF-450 and CF-600. However, sp C \equiv N has disappeared for CF-900, which is in good agreement with EDXS and XPS results, indicating that N-content is low. The curvature peak can be attributed to the presence of carbon-onion like structures as reported in Ref. [37], and it is also in good agreement with the observation of XPS peak at around 283 eV . In contrast to the frontside or porous side of foams, the noticeable changes in the backside of foams are the decrease in FWHM of D-peak from 375 to 314 cm^{-1} and the shift in G-peak position from 1564 to 1587 cm^{-1} (see Table S4 in supporting material). In summary, from both sides (porous and compact), a significant structural improvement has been noticed for carbon nanofoam upon annealing, and CF-600 is found to be an optimized sp^2 -C/ sp^3 -C ratio with appropriate amount of N-content and N-bonding.

Wettability of the electrode is one of the key factors for charge-storage performance. It has been seen that both the pristine and CF-300 are superhydrophilic (Figure 5a) in nature. The superhydrophilicity can be attributed to the huge volumetric void fraction (as estimated from the morphological information), to the presence of functional groups containing hydrogen, oxygen, and nitrogen on the surface (as obtained from elemental analysis), and to the amorphous structure with huge defect sites.[6] Moreover, higher hydrogen and nitrogen content on the carbon surface, as for the case of pristine sample (Figure 3b and 4f), leads to the formation of polar interactions and hydrogen bonding between water and the nanoform, resulting in much faster water absorption and hence the water droplet spreads spontaneously. Hence, we could not be able to record the water contact angle for the pristine sample. Similar occurrence happened for CF-300 once the water dropped on the surface, but the rate of spreading over the surface was a bit lower compared to the pristine case, which can be seen from the plots of normalized water contact angle versus evolution of droplets (Figure 5e). On the other hand, the contact angle increased with annealing temperature and nanofoams annealed at $450\text{ }^\circ\text{C}$ and above are found to be superhydrophobic in nature (Figure 5b-d). Although they are highly porous and morphologically similar to the pristine counterpart (as it can be seen in morphological analysis), the hydrophobicity can be attributed to the increased carbon to functional groups ratio (as shown from elemental analysis), improved structural quality (as seen from Raman and XPS analysis), and lowered hydrogen content (Figure 3b and 4f). At

the same time, we noticed a decrease in water contact angle with the droplet evolution time for CF-450 and CF-900, whereas it was stable for CF-600. The decrease in contact angle for CF-450 is attributed to the higher amount of hydrogen, whereas for CF-900 is due to the more abundant oxygen species (Figure 3).

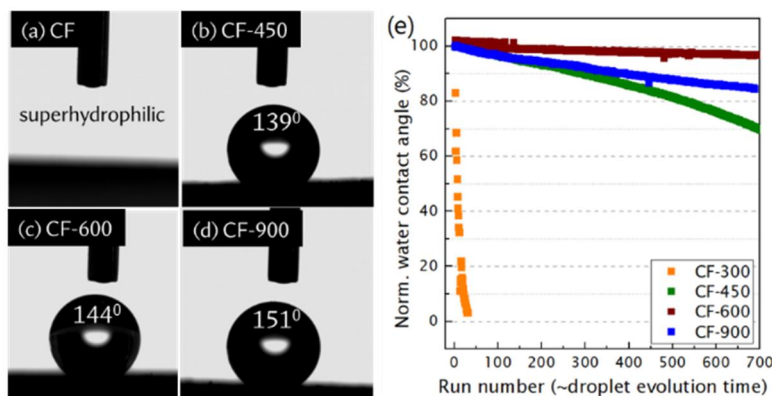


Figure 5: Static water contact angle of (a) pristine nanofoam and annealed nanofoams (b) N-a-CF-450 °C, (c) N-a-CF-600 °C, and (d) N-a-CF-900 °C. The volume of water droplet was 2 μ L. (e) Changes in water contact angle of pristine and annealed nanofoams. Run number in X-axis of (e) is equivalent to the evolution time of droplet, which is around 3 min approximately.

In order to inspect the influence of wettability and the sp^2 -C/ sp^3 -C ratio on the charge-storage performance, cyclic voltammograms (CV) for the symmetric supercapacitor device have been performed at various scan rates ranging from 0.02 to 1 V/s (Figure 6a and Figure S4a-d of supplementary material). All CV shapes are near-rectangular, mirror symmetric, and remain unchanged at various scan rates. A comparative CV of pristine and annealed carbon foams at 0.1 V/s is shown in Figure 6b. The areal capacitance is estimated and plotted in Figure 6c as a function of the scan rates. Despite the hydrophilic nature of CF-pristine and CF-300, which is preferable to have effective electrode/electrolyte interaction while used for supercapacitor applications, the lower areal capacitance and voltage of device indicate that wettability is not an influential factor for the charge-storage improvement. Moreover, a theoretical investigation reported in Ref. [38] suggests that the improvement in surface wettability leads to high energy density but it lowers the power density of the device. Based on the investigation, the observed increment in areal capacitance for the device composed of annealed foams, which are hydrophobic, is attributed to the higher but optimized sp^2/sp^3 ratio, improved structural quality, and optimized functional groups. Moreover, the voltage of the symmetric device is found to be increased from 0.6 V for pristine to 1.1 V for CF-900, although pristine NF contains higher sp^3 -carbon content. Enhancing the voltage of the device simultaneously increases the energy density and the power density (Figure S4e of supplementary Material). We have already mentioned the disappearance of the sp^3 C-H vibration for CF-450 onwards (as seen from FT-IR analysis), and the reduction in H-content indicating the transformation of sp^3 C-H to sp^3 C-C along with the increase of sp^2/sp^3 ratio. Moreover, sp^3 -bonded carbon (diamond) is well known to stabilize the widened voltage.[8][9] As a result, we have seen enhanced voltage of device with CF-900.

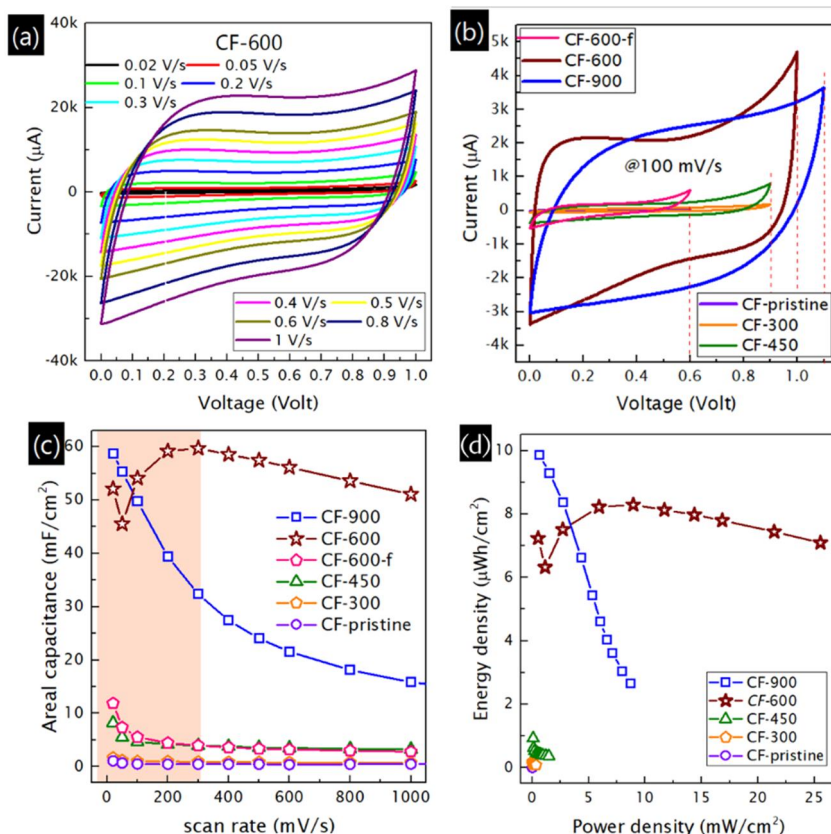


Figure 6: Supercapacitor performance of a symmetric device. (a) Cyclic voltammogram of N-a-CF-600 device at various scan rates ranging from 0.02 to 1 V/s, (b) comparative voltammograms at 0.1 V/s, (c) areal capacitance as a function of the scan rate, (d) plot of energy density vs. power density of all studied devices.

At the lowest scan rate (0.02 V/s), the highest areal capacitance of 58.7 mF/cm² is achieved for CF-900 device (Figure 6c). While compared at the scan rate of 0.1 V/s, the highest areal capacitance obtained for CF-600 device is 54.1 mF/cm² (volumetric capacitance of 4.7 F/cm³ and gravimetric capacitance of 137 F/g) and showed excellent retention at 1 V/s (51 mF/cm²). On the other hand, CF-900 device exhibited very poor rate performance at 1 V/s (32% against the capacitance at 0.1 V/s, Figure 6c), which could be due to higher amount of oxygen functional groups and negligible N-bonding despite higher sp^2/sp^3 ratio compared to CF-600. Moreover, CF-600 showed higher energy density at higher power density compared to all other devices, as shown in Figure 6d. To check the influence of wettability, we also functionalized the CF-600 by 8M HNO₃ treatment (CF-600-f) and the surface was found to be superhydrophilic as obtained from the water contact angle measurement (similar to Figure 5a, and hence no image is shown here). From the cyclic voltammogram, the maximum obtained areal capacitance was 11.8 mF/cm² at 20 mV/s, and the stable operating voltage was 0.6 V only. It has been also reported that activated carbons with higher amount of functionalities exhibited the smallest anodic electrochemical stable window in organic electrolytes.[39] After functionalization, the O/C ratio, as estimated from EDXS, increased from 1.95% to 22.1% (Figure 7a). Moreover, an increase of H-content in annealed nanofoam after HNO₃ treatment was evidenced from the change in the normalized photoluminescence slope of corresponding Raman spectra. The normalized PL slope of annealed nanofoam increased from 0.5 μm to 1.0 μm after HNO₃-treatment, reflecting an increment of hydrogen species in the structure. This result is in good agreement with the previous reports on the carbon structure after HNO₃-treatment.[40] Also changes in FWHM and position of G-peak (Figure 7b) were observed after functionalization. From FT-IR of CF-600-f (Figure 7c), a stronger C=O stretching peak relative to the C=C stretching peak was observed in nanofoam after functionalization. Thus, the additional and inappropriate oxygen and hydrogen functional groups were found to be detrimental as they lower the stable voltage of device. On the other hand, they reduce the areal capacitance of the activated device, since the excess oxygen functional groups may block the pores of carbon nanofoams.

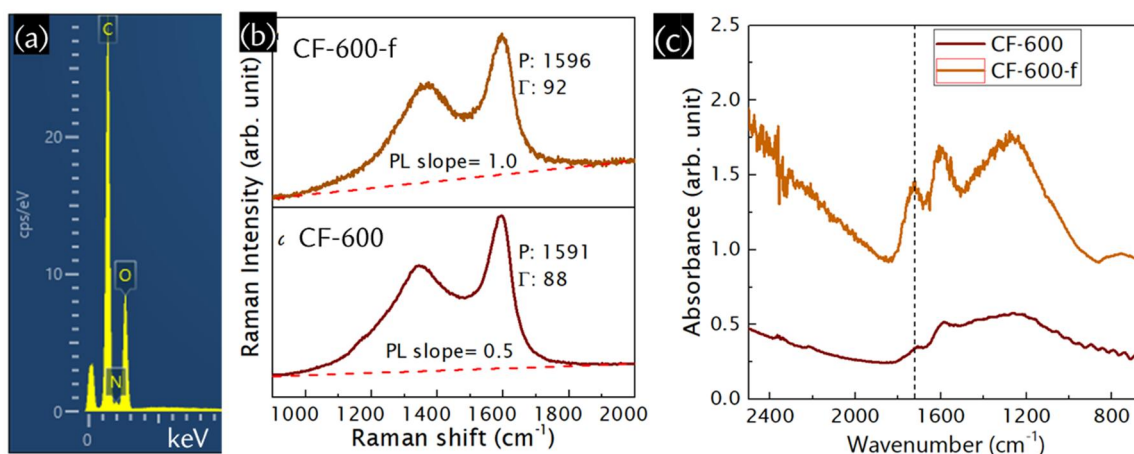


Figure 7: (a) Energy dispersive X-ray spectra, (b) Raman spectra (acquired with 514 nm exciting laser), and (c) FT-IR spectra of functionalized CF-600 (CF-600-f) after HNO_3 -treatment. In (b-c), the spectra of CF-600 are added to show the direct comparison after functionalization.

The areal capacitance of our ultrathick carbon foam device (CF-600, thickness $\sim 57 \mu\text{m}$) was found to be higher than that of symmetric supercapacitors made of superwetted vertical graphene nanosheets (2 mF/cm^2 at 100 mV/s , thickness of single electrode around 415 nm)[20], turbostratic graphene (8.2 mF/cm^2 at 50 mV/s)[41], carbon/(metal:Ti, V) oxynitride nanofoams ($0.61\text{-}1.85 \text{ mF/cm}^2$ at 100 mV/s)[42], $(\text{Fe,Mn})_3\text{O}_4$ spinel oxide thin films (15.5 mF/cm^2 at 10 mV/s , thickness of single electrode around $1 \mu\text{m}$),[21], $\text{TiO}_x\text{N}_{1-x}$ nanogrid ($\sim 5 \text{ mF/cm}^2$ at 10 mV/s)[28], cumulene *sp*-carbon/polymer composite (2.4 mF/cm^2 at 20 mV/s , thickness of single electrode $\sim 40 \mu\text{m}$)[43] and so on. While comparing the areal capacitance of electrodes (considering the electrode capacitance = $4 \times$ device capacitance, which is 216.4 mF/cm^2), the areal capacitance of CF-600 electrode is found to be much higher than that reported for electrode materials (where areal capacitance was estimated from 3-electrode configuration, mostly) such as bismuth ferrite/graphene nanocomposite (9 mF/cm^2 at 10 mV/s)[44], boron-doped ultranano- and micro-crystalline diamond (784 and $852 \mu\text{F/cm}^2$ at 20 mV/s , respectively)[45], vertical graphenes ($470 \mu\text{F/cm}^2$ at 100 mV/s), MnO_2 coated vertical graphene (118 mF/cm^2 at 100 mV/s), ZnO/Carbon nanowalls shell/core nanostructures (1.4 mF/cm^2 at 10 mV/s), Fe_2O_3 nanorice coated vertical graphenes (151 mF/cm^2 at 100 mV/s)[46], TiO_xN_y (62 mF/cm^2 at 1 mA/cm^2)[47], TiNbN (59.3 mF/cm^2 at 1.0 mA/cm^2), TiN (26.9 mF/cm^2 at 1.0 mA/cm^2)[48], NbN (39.6 mF/cm^2 at 1.0 mA/cm^2)[48], and many other thin film electrodes[3].

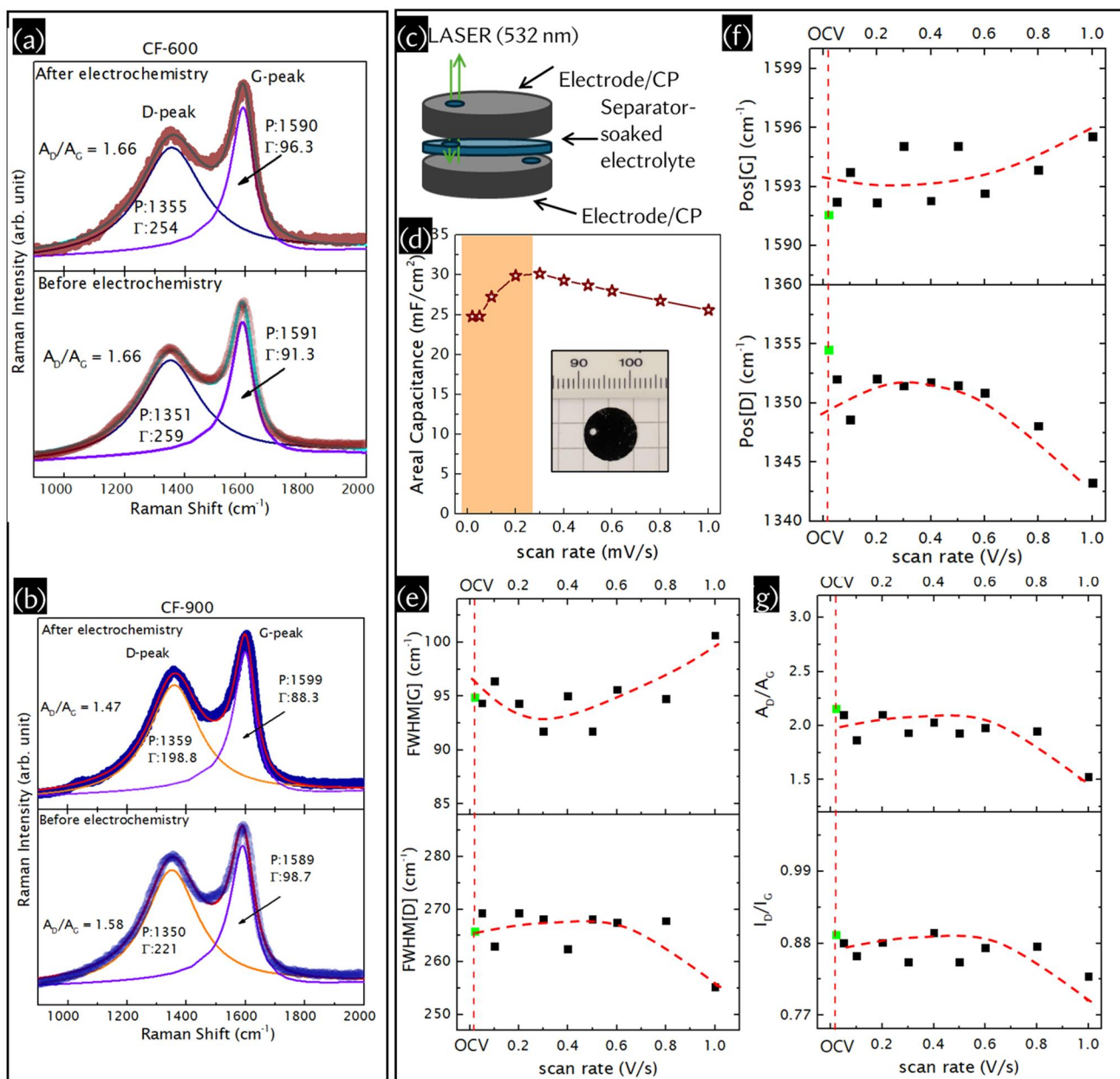


Figure 8: Raman spectra of (a) CF-600 and (b) CF-900 before and after electrochemical investigation using 514 nm laser. (c-g) *In-situ* spectro-electrochemical investigations of CF-600 using the 532 nm laser. (c) Schematic setup of the assembled device for the *in-situ* analysis, (d) scan rate-dependent areal capacitance of the device during the *in-situ* measurement with the electrode photograph in the inset, changes in (e) FWHM of D-peak and G-peak, (f) position of D-peak and G-peak, and (g) intensity ratio and area ratio of D-to-G peaks as a function of the scan rate. The substrate for the nanofoam here is carbon paper as it was used for electrochemical tests. In panels (d-g), the dashed red line is guided to show the changes without any fitting and the green square data point represent the extracted Raman parameters at the open circuit voltage (OCV) of the as-fabricated device.

The initial increase of the rate performance of CF-600 device at the scan rates ranging from 0.02 V/s to 0.3 mV/s, as highlighted in Figure 6c, is surprising, although all the electrodes were dipped into the electrolyte overnight and CV was carried out for several scan rates within the electrochemical stable window prior to recording the data mentioned here. This initial enhancement is hardly seen in literature, but it was also observed for nanoporous gold/MnO₂ hybrid electrode[22], MnO₂ nanorods on carbon nanotubes,[23] and metal-free MXene[24]. However, no explanation was provided behind the enhancement. There may be electrochemical activation-induced structural changes during the charge/discharge process, which is often observed at the initial cycles of prolonged charge-discharge tests.[5] To shed light on it, we recorded the Raman spectra for the CF-600 and CF-900 after electrochemical investigation and compared with their pristine counterparts (Figure 8a-b). For this, we disassembled the cell and the electrode materials were washed several times by deionized water to remove the electrolyte ions residues. It has been seen that the D-peak position is shifted towards higher

wavenumbers and the FWHM of the G-peak increases after the electrochemical process, indicating an electrochemical activation that induces structural changes in the nanofoam. On the other hand, the changes in Raman-extracted parameters are much higher for CF-900 after the electrochemical process. Eventually, a reduction in FWHM of D- and G-peaks, and in A_D/A_G was observed, whereas position of both peaks shifted to higher wavenumbers. To deepen the understanding over the increase in areal capacitance with respect to the scan rate for CF-600 device, we designed a setup for *in-situ* spectro-electrochemical measurements (Figure 8c, see the details in the Experimental Section). After stability tests of the device (20 cycles CV run at 0.1 V/s), the Raman spectra of the bottom electrode (the photographic image of the electrode for *in-situ* measurements is provided in the inset of Figure 8c) were recorded after four scans at each scan rate. The CVs at different scan rates are provided in Figure S5(a) and the corresponding Raman spectra are given in Figure S5b of supplementary material. We have detected similar phenomena of initial increase in areal capacitance with scan rate from the *in-situ* measurements as well (Figure 8d), indicating the consistency of our result. We deconvoluted each Raman spectrum and the results in terms of peak position and FWHM of D- and G- peaks, intensity ratio (I_D/I_G), and area ratio (A_D/A_G) are provided in Figure 8e-g. The observed changes in those parameters indicate a change in graphitic quality of nanofoam.[35] Thus the changes of those parameters between the as-fabricated device and the device scanned up to certain scan rate is attributed to the electrochemical activation-induced structural changes of the carbon nanofoam.

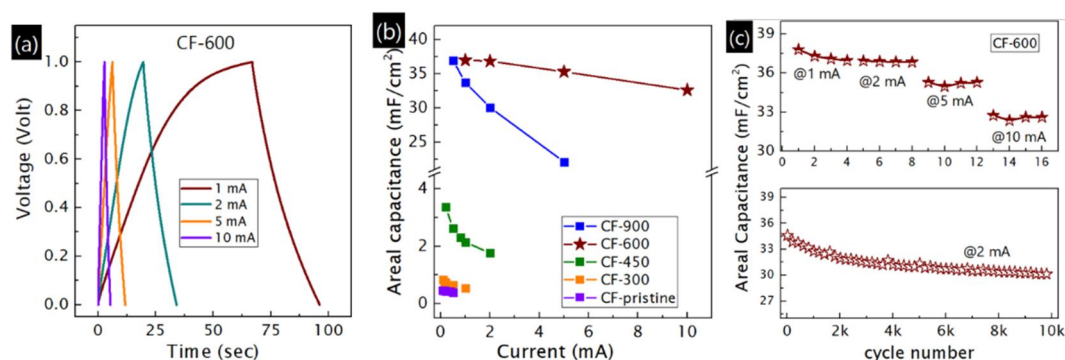


Figure 9: (a) Charge-discharge profiles of CF-600 symmetric device. (b) Estimated areal capacitance of all the studied devices with respect to the applied current. Different current was applied to the different nanofoams since they have different capacitance. (c) Rate performance at different currents and cycle stability of CF-600 symmetric supercapacitor device.

The charge-discharge profiles of all the studied devices are shown in Figure 9a and Figure S6a-d of supplementary material. Like CV, the linear triangular and symmetric charge discharge profile is obtained for all the studied samples. The highest electrochemical stable window for pristine, CF-300, CF-450, CF-600, and CF-900 is found to be 0.6, 0.9, 0.9, 1.1, and 1.2 V (Figure S6e), respectively. However, increasing the voltage of device lower the Coulombic efficiency. For instant, at the current of 1 mA, the Coulombic efficiency of CF-900 supercapacitor with voltage of 1.2 V dropped down to 84.5% from 94% for the device with voltage of 0.9 V. The areal capacitance of CF-300, CF-450, CF-600, and CF-900 supercapacitor was estimated to be 0.54, 2.15, 37.0, and 33.6 mF/cm² at 1 mA, respectively. Compared to the CF-900, the CF-600 device showed higher capacitance retention even at higher current (Figure 9b). Figure 9c shows the rate performance and the cycle stability of the CF-600 supercapacitor, indicating its capability to retain 87% of its initial capacitance after 10,000 charge-discharge cycles. The cycle test of other samples was carried out at different currents (based on the charge-storage performance) and shown in Figure S6f of supplementary material. Lastly, at the frequency of 120 Hz, CF-600 device also shows higher double layer capacitance (4.7 mF/cm²) compared to that of CF-900 device (1.2 mF/cm²) (Figure 10a). Thus it can be concluded that better ionic intercalation takes place into the CF-600.

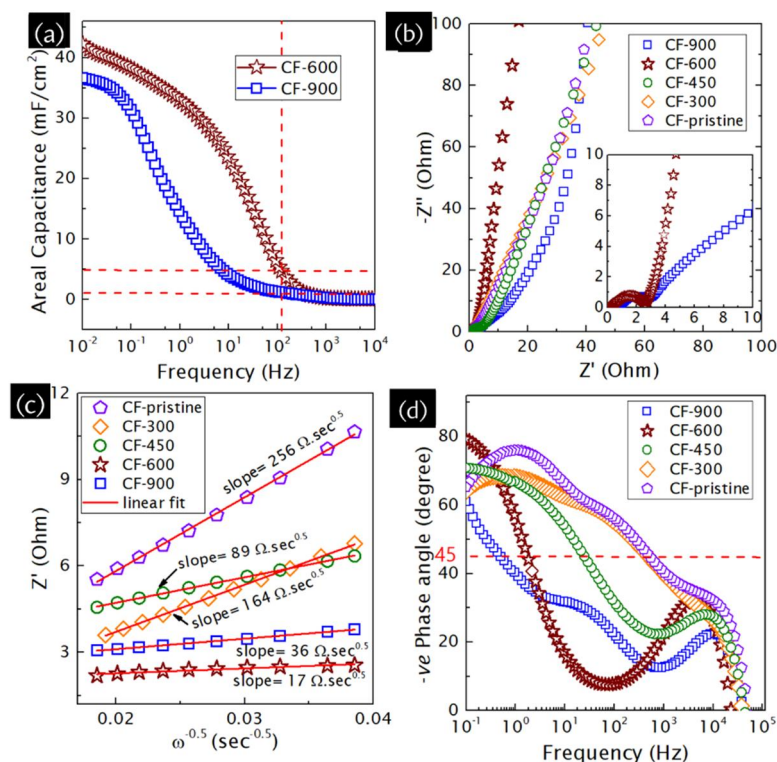


Figure 10: Electrochemical impedance spectra of devices. (a) Nyquist plots, (b) plots of Z'' vs $\omega^{-0.5}$, (c) Bode plots, and (d) variation of areal capacitance with respect to the frequency.

The charge-storage kinetics of the studied devices were investigated by electrochemical impedance spectroscopy and shown in Figure 10. From the real vs. imaginary part of impedance, known as Nyquist plot (Figure 10b, magnified version of high-frequency region in the inset), it is confirmed that the CF-600 shows the ideal supercapacitor features compared to other devices as the Nyquist line is more vertical in the mid- and low-frequency region. The real part of impedance (Z') is the combined effect of ion migration, electrical conduction, and ion diffusion. For supercapacitor, ion migration takes place at low-frequency region (below 100 Hz), whereas the ion diffusion occurs in the region of mid-frequency.[49] Hence, we estimated the ionic diffusion coefficient or Warburg coefficient (σ) from the slope of Z' vs. $\omega^{-0.5}$ plot (Figure 10c).[50] The estimated σ -values of CF-pristine, CF-300, CF-450, CF-600, and CF-900 are $256 \Omega/s^{0.5}$, $164 \Omega/s^{0.5}$, $89 \Omega/s^{0.5}$, $17 \Omega/s^{0.5}$, and $36 \Omega/s^{0.5}$, respectively, indicating better ion diffusion in CF-600. The better ion diffusion is attributed to the structural properties of CF-600, as discussed before. The frequency-dependent negative phase angle, known as Bode plot, of all studied devices is provided in Figure 10d, which can be categorized into the capacitive, diffusive, and resistive part in the low-frequency, mid-frequency, and high-frequency ranges, respectively. At -45° , the characteristic frequencies (time constants) of CF-600 and CF-900, obtained from the corresponding Bode plots, are 3.72 Hz (0.27 s) and 0.58 Hz (1.72 s). The higher the frequency at -45° , the faster the charge-discharge rate of device is.

4. Conclusion

In summary, binder-free and conductive-free amorphous carbon nanofoam was synthesized by pulsed laser deposition at room temperature, and the sp^2 -C/ sp^3 -C ratio and wettability were properly tuned by vacuum annealing treatment. Raman and FT-IR spectroscopic results, wettability measurements, and electrochemical charge-storage performances suggested that the hydrophobic nanofoam with optimized sp^2/sp^3 ratio and appropriate amount of N-content with specific N-bonds was crucial to exhibit the highest areal capacitance of 51 mF/cm^2 at 0.1 V/s, with excellent capacitance retention compared to its pristine hydrophilic counterpart and to hydrophobic nanofoams with higher sp^2/sp^3 -content and lower functional groups. Eventually, the hydrophobic nanofoam with optimized structure not only delivered higher capacitance, but also a widened voltage of the device, and hence a higher energy density. Moreover, the initial capacitance enhancement of the optimized structure as a function of the scan rate was investigated by *in-situ* Raman spectro-electrochemistry,

indicating electrochemical activation-induced structural changes during the charge-discharge process. These results demonstrate the potentials of porous, lightweight, and binder-free nanofoam electrode for the next-generation macro- to micro- energy storage devices.

Authors contributions

S.G., V.R., and C. S. C. planned and conceptualized the work. S. G. and G. P. did the synthesis and characterizations of the materials. A. M. assisted in spectro-electrochemistry experiment. A. C. and G. B. did the XPS measurement. A. L. performed the FT-IR measurement, and M. T. helped in interpreting the result. R. S. did the wettability measurement. C. C., V. R. and A. L. B. helped in data analysis and interpretation. S. G. wrote the manuscript. All authors edited the manuscript and approved the final version of the manuscript.

Notes

The authors declare no competing financial interest.

ACKNOWLEDGEMENT

S.G thank European commissions for the Marie Skłodowska-Curie Fellowship (grant no. 101067998-ENHANCER) and SEED fund from Department of Energy, Politecnico di Milano. Carlo S. Casari acknowledges partial funding from the European Research Council (ERC) under the European Union's Horizon 2020 Research and Innovation Program ERC Consolidator Grant (ERC CoG2016 EspLORE Grant Agreement 724610, website: www.esplora.polimi.it). Carlo S. Casari also acknowledges funding by the project funded under the National Recovery and Resilience Plan (NRRP), Mission 4 Component 2 Investment 1.3 Call for Tender 1561 of 11.10.2022 of Ministero dell'Università e della Ricerca (MUR), funded by the European Union NextGenerationEU Award Project Code PE0000021, Concession Decree 1561 of 11.10.2022 adopted by Ministero dell'Università e della Ricerca (MUR), CUP D43C22003090001, Project "Network 4 Energy Sustainable Transition (NEST)". Agnieszka Jastrzebska kindly acknowledges funding from Warsaw University of Technology within the Excellence Initiative: Research University (IDUB) programme. C. C. acknowledge support by the UKRI (Grant EP/X028844/1). We would like to thank N. G. Krishna for useful discussion on XPS result.

DATA AVAILABILITY: All data of this study are available in the main manuscript and Supplementary Information.

References:

- [1] S.V. Sadavar, S. Lee, S. Park, Advancements in Asymmetric Supercapacitors: From Historical Milestones to Challenges and Future Directions, *Adv. Sci.* 11 (2024) 2403172. <https://doi.org/10.1002/advs.202403172>.
- [2] N.R. Chodankar, S. V. Karekar, M. Safarkhani, A.M. Patil, P.A. Shinde, R.B. Ambade, J. Kim, Y. Han, Y. Huh, A. al Ghaferi, E. Alhajri, Revolutionizing Implantable Technology: Biocompatible Supercapacitors as the Future of Power Sources, *Adv. Funct. Mater.* 34 (2024) 2406819. <https://doi.org/10.1002/adfm.202406819>.
- [3] J. Cheng, B. Mi, Q. Wang, H. Wang, T. Zhou, Y. Li, H. Hou, Y. Zhu, Research on magnetron sputtering thin films as electrode materials for supercapacitors, *Chem. Eng. J.* 509 (2025) 161242. <https://doi.org/10.1016/j.cej.2025.161242>.
- [4] S. Ghosh, S. Barg, S.M. Jeong, K.K. Ostrikov, Heteroatom-Doped and Oxygen-Functionalized Nanocarbons for High-Performance Supercapacitors, *Adv. Energy Mater.* 10 (2020) 2001239. <https://doi.org/10.1002/aenm.202001239>.
- [5] S. Ghosh, S.R. Polaki, A. Macrelli, C.S. Casari, S. Barg, S.M. Jeong, K. (Ken) Ostrikov, Nanoparticle-enhanced multifunctional nanocarbons—recent advances on electrochemical energy storage applications, *J. Phys. D: Appl. Phys.* 55 (2022) 413001. <https://doi.org/10.1088/1361-6463/ac7bb5>.
- [6] L. Zhao, Y. Li, M. Yu, Y. Peng, F. Ran, Electrolyte-Wettability Issues and Challenges of Electrode

- Materials in Electrochemical Energy Storage, Energy Conversion, and Beyond, *Adv. Sci.* 10 (2023) 2300283. <https://doi.org/10.1002/advs.202300283>.
- [7] M.F. El-Kady, V. Strong, S. Dubin, R.B. Kaner, Laser Scribing of High-Performance and Flexible Graphene-Based Electrochemical Capacitors, *Science* (80-.). 335 (2012) 1326–1330. <https://doi.org/10.1126/science.1216744>.
- [8] S. Deshmukh, S. Kunuku, P. Jakobczyk, A. Olejnik, C. Chen, H. Niu, B. Yang, N. Yang, R. Bogdanowicz, Diamond-Based Supercapacitors with Ultrahigh Cyclic Stability Through Dual-Phase MnO₂ - Graphitic Transformation Induced by High-Dose Mn-Ion Implantation, *Adv. Funct. Mater.* 34 (2024) 2308617. <https://doi.org/10.1002/adfm.202308617>.
- [9] K. Siuzdak, R. Bogdanowicz, Nano-engineered Diamond-based Materials for Supercapacitor Electrodes: A Review, *Energy Technol.* 6 (2018) 223–237. <https://doi.org/10.1002/ente.201700345>.
- [10] B. Chen, Z. Zhai, N. Huang, C. Zhang, S. Yu, L. Liu, B. Yang, X. Jiang, N. Yang, Highly Localized Charges of Confined Electrical Double-Layers Inside 0.7-nm Layered Channels, *Adv. Energy Mater.* 13 (2023) 2300716. <https://doi.org/10.1002/aenm.202300716>.
- [11] X. Liu, D. Lyu, C. Merlet, M.J.A. Leesmith, X. Hua, Z. Xu, C.P. Grey, A.C. Forse, Structural disorder determines capacitance in nanoporous carbons, *Science* (80-.). 384 (2024) 321–325. <https://doi.org/10.1126/science.adn6242>.
- [12] J. Chmiola, G. Yushin, Y. Gogotsi, C. Portet, P. Simon, P.L. Taberna, Anomalous Increase in Carbon Capacitance at Pore Sizes Less Than 1 Nanometer, *Science* (80-.). 313 (2006) 1760–1763. <https://doi.org/10.1126/science.1132195>.
- [13] T. Wang, R. Pan, M.L. Martins, J. Cui, Z. Huang, B.P. Thapaliya, C.-L. Do-Thanh, M. Zhou, J. Fan, Z. Yang, M. Chi, T. Kobayashi, J. Wu, E. Mamontov, S. Dai, Machine-learning-assisted material discovery of oxygen-rich highly porous carbon active materials for aqueous supercapacitors, *Nat. Commun.* 14 (2023) 4607. <https://doi.org/10.1038/s41467-023-40282-1>.
- [14] G. Sahoo, S.R. Polaki, S. Ghosh, N.G. Krishna, M. Kamruddin, K. (Ken) Ostrikov, Plasma-tuneable oxygen functionalization of vertical graphenes enhance electrochemical capacitor performance, *Energy Storage Mater.* 14 (2018) 297–305. <https://doi.org/10.1016/j.ensm.2018.05.011>.
- [15] S. Gadipelli, H. Akbari, J. Li, C.A. Howard, H. Zhang, P.R. Shearing, D.J.L. Brett, Structure-guided Capacitance Relationships in Oxidized Graphene Porous Materials Based Supercapacitors, *ENERGY Environ. Mater.* 6 (2023) e12637. <https://doi.org/10.1002/eem2.12637>.
- [16] S.H. Tamboli, B.S. Kim, G. Choi, H. Lee, D. Lee, U.M. Patil, J. Lim, S.B. Kulkarni, S. Chan Jun, H.H. Cho, Post-heating effects on the physical and electrochemical capacitive properties of reduced graphene oxide paper, *J. Mater. Chem. A* 2 (2014) 5077. <https://doi.org/10.1039/c4ta00209a>.
- [17] S. Matsushita, B. Yan, T. Matsui, J.-D. Kim, K. Akagi, Conjugated polymer-based carbonaceous films as binder-free carbon electrodes in supercapacitors, *RSC Adv.* 8 (2018) 19512–19523. <https://doi.org/10.1039/C8RA00267C>.
- [18] I. Kim, C. Shim, S.W. Kim, C. Lee, J. Kwon, K. Byun, U. Jeong, Amorphous Carbon Films for Electronic Applications, *Adv. Mater.* 35 (2023) 2204912. <https://doi.org/10.1002/adma.202204912>.
- [19] S. Ghosh, M. Righi, A. Macrelli, G. Divitini, D. Orecchia, A. Maffini, F. Goto, G. Bussetti, D. Dellasega, V. Russo, A. Li Bassi, C.S. Casari, Ballistic-Aggregated Carbon Nanofoam in Target-Side of Pulsed Laser Deposition for Energy Storage Applications, *ChemSusChem*. 17 (2024) 202400755. <https://doi.org/10.1002/cssc.202400755>.
- [20] G. Sahoo, S.R. Polaki, S. Ghosh, N.G. Krishna, M. Kamruddin, Temporal-stability of plasma functionalized vertical graphene electrodes for charge storage, *J. Power Sources*. 401 (2018) 37–48. <https://doi.org/10.1016/j.jpowsour.2018.08.071>.
- [21] B. Jolayemi, G. Buvat, T. Brousse, P. Roussel, C. Lethien, Sputtered (Fe,Mn) 3 O 4 Spinel Oxide Thin Films for Micro-Supercapacitor, *J. Electrochem. Soc.* 169 (2022) 110524. <https://doi.org/10.1149/1945-7111/aca050>.
- [22] X. Lang, A. Hirata, T. Fujita, M. Chen, Nanoporous metal/oxide hybrid electrodes for electrochemical supercapacitors, *Nat. Nanotechnol.* 6 (2011) 232–236. <https://doi.org/10.1038/nnano.2011.13>.
- [23] S. Bouachma, X. Zheng, A. Moreno Zuria, M. Kechouane, N. Gabouze, M. Mohamedi, Enhanced

- Supercapacitor and Cycle-Life Performance: Self-Supported Nanohybrid Electrodes of Hydrothermally Grown MnO₂ Nanorods on Carbon Nanotubes in Neutral Electrolyte, *Materials* (Basel). 17 (2024) 4079. <https://doi.org/10.3390/ma17164079>.
- [24] H. Xue, P. Huang, L. Lai, Y. Su, A. Strömberg, G. Cao, Y. Fan, S. Khartsev, M. Göthelid, Y. Sun, J. Weissenrieder, K.B. Gylfason, F. Niklaus, J. Li, High-rate metal-free MXene microsupercapacitors on paper substrates, *Carbon Energy*. 6 (2024) e442. <https://doi.org/10.1002/cey2.442>.
- [25] M.-C. Liu, L.-B. Kong, P. Zhang, Y.-C. Luo, L. Kang, Porous wood carbon monolith for high-performance supercapacitors, *Electrochim. Acta*. 60 (2012) 443–448. <https://doi.org/10.1016/j.electacta.2011.11.100>.
- [26] M.K. Hoque, J.A. Behan, J. Creel, J.G. Lunney, T.S. Perova, P.E. Colavita, Reactive Plasma N-Doping of Amorphous Carbon Electrodes: Decoupling Disorder and Chemical Effects on Capacitive and Electrocatalytic Performance, *Front. Chem.* 8 (2020) 593932. <https://doi.org/10.3389/fchem.2020.593932>.
- [27] A. Ciszewski, B. Rydyńska, Studies on self-assembly phenomena of hydrophilization of microporous polypropylene membrane by acetone aldol condensation products: New separator for high-power alkaline batteries, *J. Power Sources*. 166 (2007) 526–530. <https://doi.org/10.1016/j.jpowsour.2007.01.034>.
- [28] Z. Wang, Z. Li, Z. Zou, Application of binder-free TiO_xN_{1-x} nanogrid film as a high-power supercapacitor electrode, *J. Power Sources*. 296 (2015) 53–63. <https://doi.org/10.1016/j.jpowsour.2015.07.040>.
- [29] D. Haberer, C.E. Giusca, Y. Wang, H. Sachdev, A. V. Fedorov, M. Farjam, S.A. Jafari, D. V. Vyalikh, D. Usachov, X. Liu, U. Treske, M. Grobosch, O. Vilkov, V.K. Adamchuk, S. Irle, S.R.P. Silva, M. Knupfer, B. Büchner, A. Grüneis, Evidence for a New Two-Dimensional C₄H-Type Polymer Based on Hydrogenated Graphene, *Adv. Mater.* 23 (2011) 4497–4503. <https://doi.org/10.1002/adma.201102019>.
- [30] F. Zhao, Y. Raitses, X. Yang, A. Tan, C.G. Tully, High hydrogen coverage on graphene via low temperature plasma with applied magnetic field, *Carbon N. Y.* 177 (2021) 244–251. <https://doi.org/10.1016/j.carbon.2021.02.084>.
- [31] S. Ghosh, S.K. Behera, A. Mishra, C.S. Casari, K.K. Ostrikov, Quantum Capacitance of Two-Dimensional-Material-Based Supercapacitor Electrodes, *Energy & Fuels*. 37 (2023) 17836–17862. <https://doi.org/10.1021/acs.energyfuels.3c02714>.
- [32] C.V. Raman, A new radiation, *Indian J. Phys.* 2 (1928) 387–398.
- [33] C. Casiraghi, A.C. Ferrari, J. Robertson, Raman spectroscopy of hydrogenated amorphous carbons, *Phys. Rev. B*. 72 (2005) 085401. <https://doi.org/10.1103/PhysRevB.72.085401>.
- [34] A.C. Ferrari, S.E. Rodil, J. Robertson, Interpretation of infrared and Raman spectra of amorphous carbon nitrides, *Phys. Rev. B*. 67 (2003) 155306. <https://doi.org/10.1103/PhysRevB.67.155306>.
- [35] A.C. Ferrari, J. Robertson, Interpretation of Raman spectra of disordered and amorphous carbon, *Phys. Rev. B*. 61 (2000) 14095–14107. <https://doi.org/10.1103/PhysRevB.61.14095>.
- [36] R.N. Tarrant, D.R. McKenzie, M.M.M. Bilek, Raman characterisation of PIII multilayer carbon films, *Diam. Relat. Mater.* 13 (2004) 1422–1426. <https://doi.org/10.1016/j.diamond.2004.01.028>.
- [37] D. Roy, M. Chhowalla, N. Hellgren, T.W. Clyne, G.A.J. Amaratunga, Probing carbon nanoparticles in CN_x thin films using Raman spectroscopy, *Phys. Rev. B*. 70 (2004) 035406. <https://doi.org/10.1103/PhysRevB.70.035406>.
- [38] S. Zhao, Z. Song, L. Qing, J. Zhou, C. Qiao, Surface Wettability Effect on Energy Density and Power Density of Supercapacitors, *J. Phys. Chem. C*. 126 (2022) 9248–9256. <https://doi.org/10.1021/acs.jpcc.2c01455>.
- [39] Z. Ding, V. Trouillet, S. Dsoke, Are Functional Groups Beneficial or Harmful on the Electrochemical Performance of Activated Carbon Electrodes?, *J. Electrochem. Soc.* 166 (2019) A1004–A1014. <https://doi.org/10.1149/2.0451906jes>.
- [40] H. Jin, X. Wang, Z. Gu, J. Polin, Carbon materials from high ash biochar for supercapacitor and improvement of capacitance with HNO₃ surface oxidation, *J. Power Sources*. 236 (2013) 285–292.

- <https://doi.org/10.1016/j.jpowsour.2013.02.088>.
- [41] N. Samartzis, K. Bhorkar, M. Athanasiou, L. Sygellou, V. Dracopoulos, T. Ioannides, S.N. Yannopoulos, Direct laser-assisted fabrication of turbostratic graphene electrodes: Comparing symmetric and zinc-ion hybrid supercapacitors, *Carbon N. Y.* 201 (2023) 941–951. <https://doi.org/10.1016/j.carbon.2022.09.076>.
- [42] S. Ghosh, G. Pagani, M. Righi, C. Hou, V. Russo, C.S. Casari, One-step pulsed laser deposition of carbon/metal oxynitride composites for supercapacitor application, *J. Phys. D: Appl. Phys.* 57 (2024) 495305. <https://doi.org/10.1088/1361-6463/ad76bc>.
- [43] S. Ghosh, M. Righi, S. Melesi, Y. Qiu, R.R. Tykwinski, C.S. Casari, Cumulenic sp-Carbon atomic wires wrapped with polymer for supercapacitor application, *Carbon N. Y.* 234 (2025) 119952. <https://doi.org/10.1016/j.carbon.2024.119952>.
- [44] A. Soam, R. Kumar, M. C. M. Singh, D. Thatoi, R.O. Dusane, Development of paper-based flexible supercapacitor: Bismuth ferrite/graphene nanocomposite as an active electrode material, *J. Alloys Compd.* 813 (2020) 152145. <https://doi.org/10.1016/j.jallcom.2019.152145>.
- [45] S. Suman, D.K. Sharma, O. Szabo, B. Rakesh, M. Marton, M. Vojs, A. Vincze, S.P. Dutta, U. Balaji, D. Debasish, R. Sakthivel, K.J. Sankaran, A. Kromka, Vertically aligned boron-doped diamond nanostructures as highly efficient electrodes for electrochemical supercapacitors, *J. Mater. Chem. A.* 12 (2024) 21134–21147. <https://doi.org/10.1039/D3TA07728D>.
- [46] S. Ghosh, S.R. Polaki, G. Sahoo, E.-M. Jin, M. Kamruddin, J.S. Cho, S.M. Jeong, Designing metal oxide-vertical graphene nanosheets structures for 2.6 V aqueous asymmetric electrochemical capacitor, *J. Ind. Eng. Chem.* 72 (2019) 107–116. <https://doi.org/10.1016/j.jiec.2018.12.008>.
- [47] A. Ramadoss, N. Swain, G. Saravanan, S.Z. Noby, K. Kirubavathi, L. Schmidt-Mende, K. Selvaraju, Titanium oxynitride coated graphite paper electrodes for light-weight supercapacitors, *J. Mater. Sci. Mater. Electron.* 33 (2022) 9669–9678. <https://doi.org/10.1007/s10854-021-07644-1>.
- [48] B. Wei, F. Ming, H. Liang, Z. Qi, W. Hu, Z. Wang, All nitride asymmetric supercapacitors of niobium titanium nitride-vanadium nitride, *J. Power Sources.* 481 (2021) 228842. <https://doi.org/10.1016/j.jpowsour.2020.228842>.
- [49] S. Zhang, B. Li, C. Cui, W. Qian, Y. Jin, The Progress and Comprehensive Analysis of Supercapacitors for Alternating Current Line Filtering: A Review, *Batter. Supercaps.* 6 (2023). <https://doi.org/10.1002/batt.202200566>.
- [50] Y. Yuan, C. Zhan, K. He, H. Chen, W. Yao, S. Sharifi-Asl, B. Song, Z. Yang, A. Nie, X. Luo, H. Wang, S.M. Wood, K. Amine, M.S. Islam, J. Lu, R. Shahbazian-Yassar, The influence of large cations on the electrochemical properties of tunnel-structured metal oxides, *Nat. Commun.* 7 (2016) 13374. <https://doi.org/10.1038/ncomms13374>.

SUPPORTING MATERIAL

Wettability and sp^2/sp^3 ratio effects on supercapacitor performance of N-doped hydrogenated amorphous Carbon Nanofoam

Subrata Ghosh^{1,2*}, Giacomo Pagani¹, Andrea Macrelli¹, Alberto Calloni³, Gianlorenzo Bussetti³, Andrea Lucotti⁴, Matteo Tommasini⁴, Raffaella Suriano⁵, Valeria Russo¹, Agnieszka M. Jastrzębska², Cinzia Casiraghi⁶, Andrea Li Bassi¹, Carlo S. Casari^{1*}

¹ Micro and Nanostructured Materials Laboratory – NanoLab, Department of Energy, Politecnico di Milano, via Ponzio 34/3, Milano, 20133, Italy

² Faculty of Mechatronics, Warsaw University of Technology, 'sw. Andrzeja Boboli 8, 02-525 Warsaw, Poland

³ Solid Liquid Interface Nano-Microscopy and Spectroscopy (SoLINano-Σ) lab, Department of Physics, Politecnico di Milano, Piazza Leonardo da Vinci 32, 20133 Milano, Italy

⁴ Department of Chemistry, Materials and Chemical Engineering, "Giulio Natta" Politecnico di Milano, Milano, 20133, Italy

⁵ Laboratory of Chemistry and Characterization of Innovative Polymers (ChIPLab), Department of Chemistry, Materials and Chemical Engineering "Giulio Natta", Politecnico di Milano, Piazza Leonardo da Vinci 32, 20133 Milano, Italy

⁶ Department of Chemistry, University of Manchester, Manchester, M13 9PL, UK

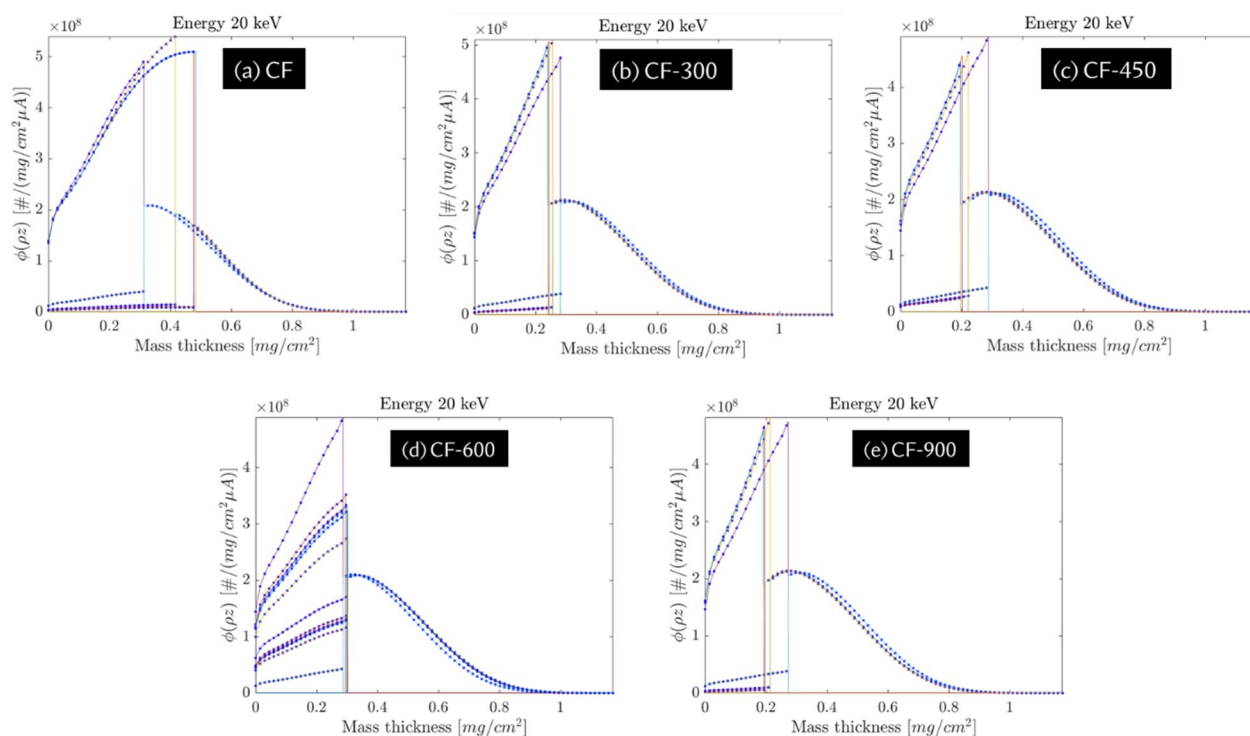


Figure S1: Simulated data of mass density calculation of (a) CF-pristine, (b) CF-300, (c) CF-450, (d) CF-600 and (e) CF-900 using EDDIE software. The y-axis of plot represents X-ray generation distribution function ($\phi(\rho_z)$) in samples and each coloured line corresponds to the iteration.

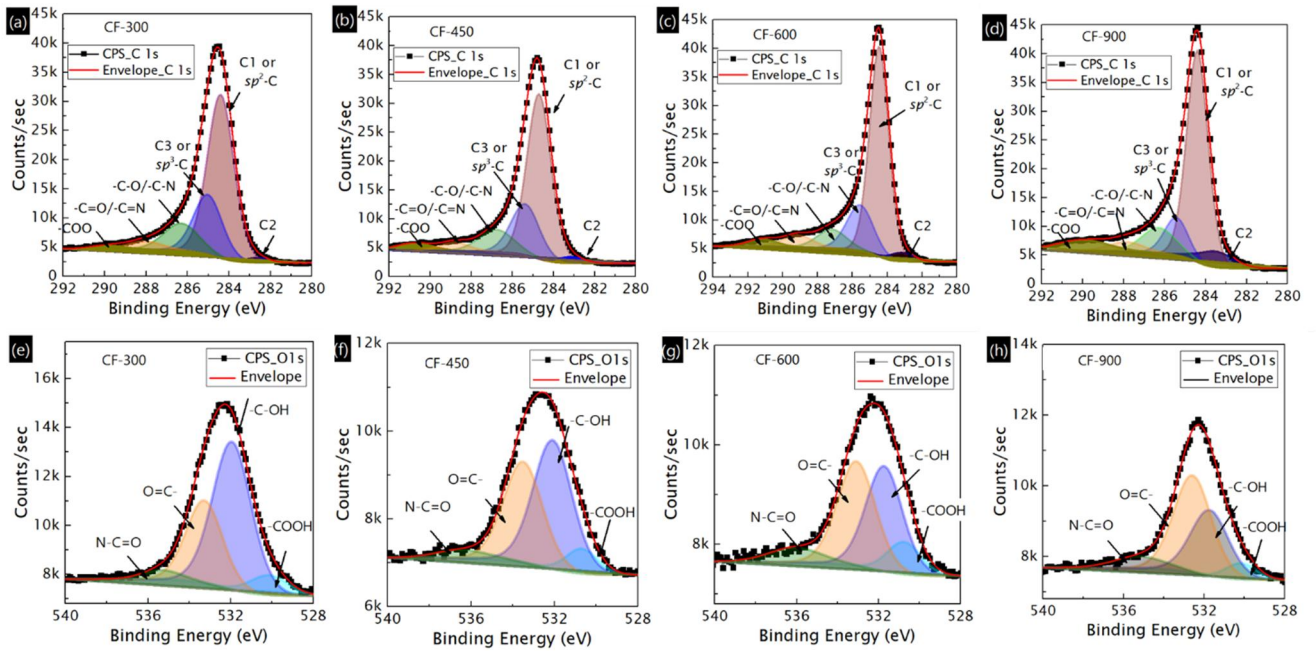


Figure S2: Top panel: XPS C1s spectra with deconvoluted peaks of (a) CF-300, (b) CF-450, (c) CF-600, and (d) CF-900. Bottom panel: XPS O1s spectra with deconvoluted peaks of (e) CF-300, (f) CF-450, (g) CF-600, and (h) CF-900.

Table S1: Extracted parameters of C1s deconvoluted XPS peaks of all studied samples.

Sample	sp^2 -C		sp^3 -C		sp^3 -C		-C-O/-C-N		-C=O/-C=N		-COO	
	B.E. (eV)	con. (%)	B.E. (eV)	con. (%)	B.E. (eV)	con. (%)	B.E. (eV)	con. (%)	B.E. (eV)	con. (%)	B.E. (eV)	con. (%)
CF	282.98	1.92	284.53	48.7	285.17	24.63	286.24	14.7	287.67	7.75	289.76	2.3
CF-300	282.62	1.52	284.4	57.64	285.01	22.7	286.3	12.7	288.06	3.77	289.82	1.68
CF-450	283.16	2.27	284.7	58.02	285.38	21	286.77	11.28	288.81	3.65	290.77	3.78
CF-600	283.16	3.08	284.46	61.38	285.56	18.29	287.18	8.42	289.14	5.48	291.18	3.34
CF-900	283.51	7.16	284.4	58.43	285.42	11.62	286.28	11.43	287.86	4.31	289.98	7.05

Table S2: Extracted parameters of N1s deconvoluted XPS peaks of all studied samples.

Sample	Pyridinic-N		Pyridinic-N		Pyridinic-N		NOx or satellite peak	
	B.E. (eV)	con. (%)	B.E. (eV)	con. (%)	B.E. (eV)	con. (%)	B.E. (eV)	con. (%)
CF	399.14	59.43	399.79	28.06	401.68	7.84	404.69	4.68
CF-300	398.87	57.96	400.03	31.99	402.61	3.95	404.99	6.1
CF-450	398.92	49.06	400.54	34.18	402.58	6.3	405.19	10.46
CF-600	398.46	37.8	400.61	41.17	402.86	10.84	405.36	10.18
CF-900	398.94	13.85	401.1	48.96	403.62	18.02	405.67	19.17

Table S3: Extracted parameters of O1s deconvoluted XPS peaks of all studied samples.

Sample	-COOH		-C-OH		O=C-		N-C=O	
	B.E. (eV)	con. (%)	B.E. (eV)	con. (%)	B.E. (eV)	con. (%)	B.E. (eV)	con. (%)
CF	530.16	6.86	532.2	50.38	533.33	40.46	535.95	2.29
CF-300	530.14	7.72	531.94	57.83	533.27	30.74	535.33	3.71
CF-450	530.69	7.82	532.09	49.38	533.5	38.71	536.46	4.09
CF-600	530.76	11.37	531.73	39.59	533.08	41.17	536.07	7.87
CF-900	530.17	6.87	531.73	34.19	532.57	50.54	535.19	8.4

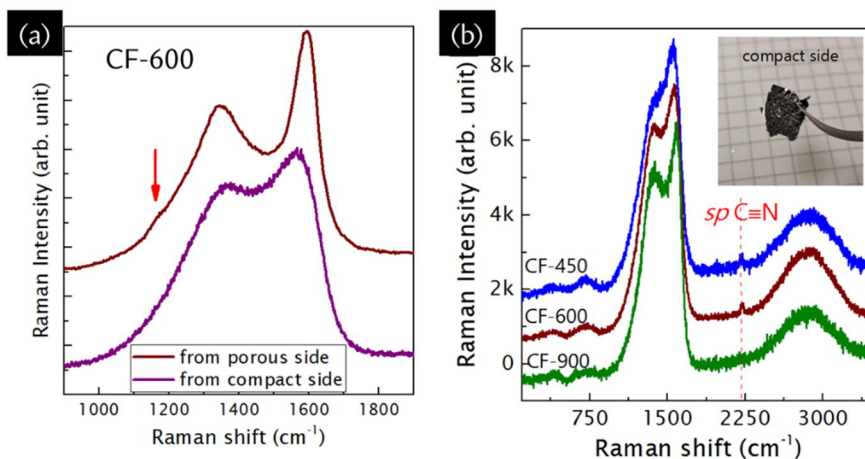


Figure S3: Raman spectra of (a) CF-600 recorded from compact side and compared with porous side, and (b) compact side of CF-450, CF-600, and CF-900 with the photographic image of film taken from compact side. Laser wavelength is 514 nm.

Table S4: Extracted Raman spectroscopic data of CF-450, CF-600, and CF-900 from the compact side.

		CF-450_compact side	CF-600_compact side	CF-900_compact side
D-peak	position (cm^{-1})	1374	1362	1372
	FWHM (cm^{-1})	375	325	314
G-peak	position (cm^{-1})	1565	1570	1587
	FWHM (cm^{-1})	151	152	123

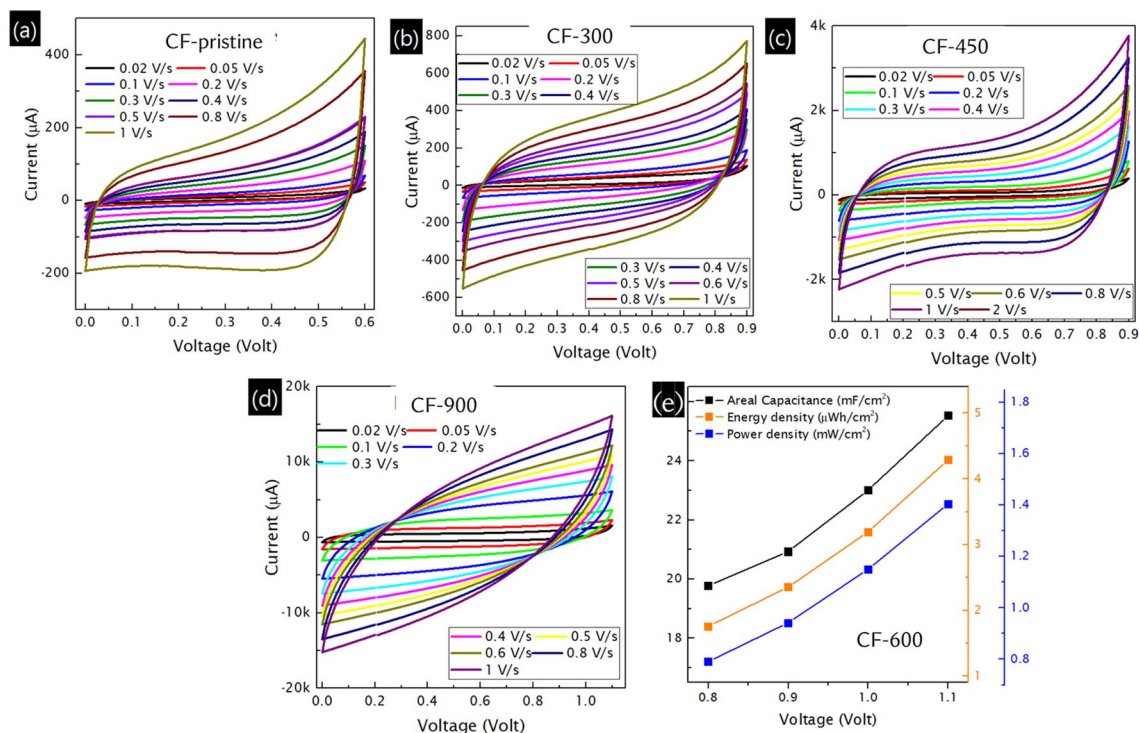


Figure S4: Cyclic voltammograms of symmetric devices made up with (a) CF-pristine, (b) CF-300, (c) CF-450, and (d) CF-900 at different scan rates ranging from 0.02 V/s to 1 V/s. (e) Plot of the areal capacitance, energy density, and power density of CF-600 device as a function of the voltage at the scan rate of 0.1 V/s.

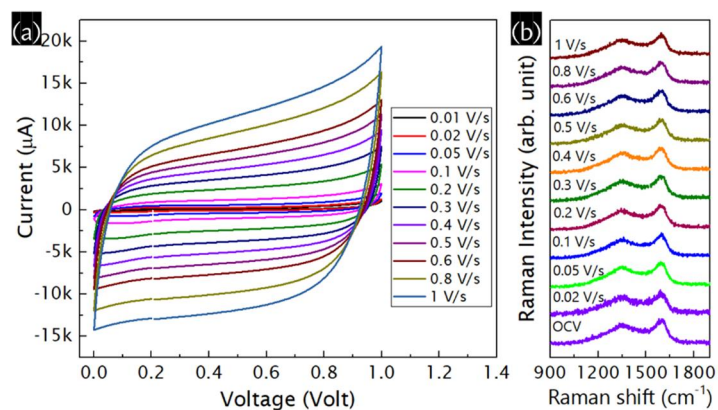


Figure S5: *In-situ* spectro-electrochemical results. The laser used to record the Raman spectra here was 532 nm and the laser power was 1.7 mW. (a) Cyclic voltammogram of the assembled device at different scan rates. (b) Normalized Raman spectra of bottom electrode at open circuit voltage and after each scan rate from 0.02 V/s to 1 V/s. Raman spectra were recorded after scanning the cyclic voltammetry four times at the specific scan rate.

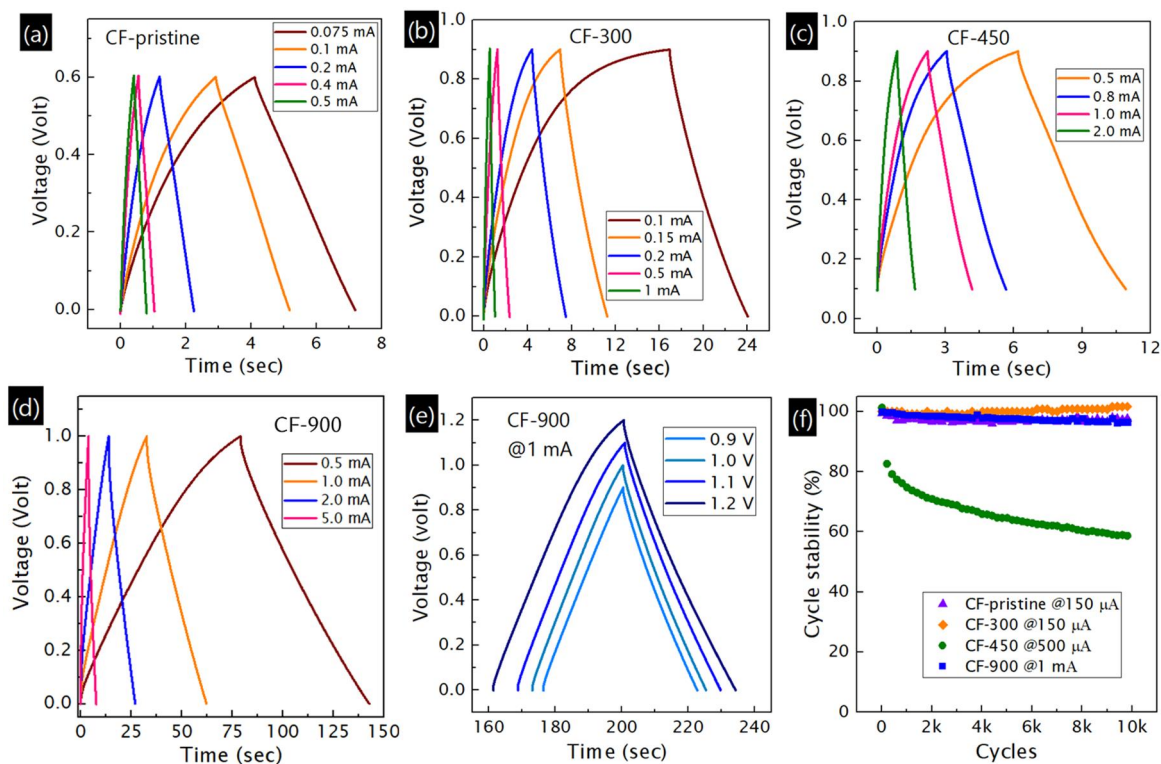


Figure S6: Charge-discharge profiles of aqueous symmetric device made with (a) CF-pristine, (b) CF-300, (c) CF-450, and (d) CF-900 at different currents. (e) Charge-discharge profile of CF-900 at different voltage. (f) Cycle stability of CF-pristine, CF-300, CF-450 and CF-900.